Cramér-Rao Bounds for Holographic Positioning

Antonio A. D'Amico, Andrea de Jesus Torres, *Member, IEEE*, Luca Sanguinetti, *Senior Member, IEEE*, and Moe Win, *Fellow, IEEE*

***Abstract*—Multiple antennas arrays combined with high carrier frequencies play a key role in wireless networks for communications but also for localization and sensing applications. To understand the fundamental limits of electromagnetically large antenna arrays for localization, this paper combines wave propagation theory with estimation theory, and computes the Cramér-Rao Bound (CRB) for the estimation of the source position on the basis of the three Cartesian components of the electric field, observed over a rectangular surface area. The problem is referred to as holographic positioning and it intrinsically depends on the radiation angular pattern of the transmitting source, which is typically ignored in standard signal processing models. We assume that the source is a Hertzian dipole, and address the holographic positioning problem in both cases, that is, with and without a priori knowledge of its orientation. To simplify the analysis and gain further insights, we also consider the case in which the dipole is located on the line perpendicular to the surface center. Numerical and asymptotic results are given to quantify the CRBs, and to quantify the effect of various system parameters on the ultimate estimation accuracy. It turns out that square surfaces with side comparable to the distance are needed to guarantee a centimeter-level accuracy in the mmWave bands. Moreover, we show that the CRBs with and without a priori knowledge of the source dipole orientation are numerically the same. The provided CRBs are also used to benchmark different maximum-likelihood estimators (MLEs) derived on the basis of a discrete representation of different models of the electric field. The analysis shows that, if the standard models are used (neglecting the radiation angular pattern), the MLE accuracy is far from the CRB. On the other hand, it approaches the CRB when the more detailed electromagnetic model is considered.**

***Index Terms*—Cramér-Rao bound, wave propagation theory, source localization, planar electromagnetic surfaces, holographic positioning.**

I. Introduction

THE estimation accuracy of signal processing algorithms for positioning is fundamentally limited by the quality of the underlying measurements. For time-based measurements, high resolution and high accuracy can only be obtained when a large bandwidth is available. Improvements can be achieved by using multiple anchor nodes, located in known positions. Antenna arrays have thus far only played a marginal role in positioning since the small arrays of today's networks provide little benefit. With future networks, the situation may change significantly. Indeed, the 5G technology standard [2] is envisioned to operate in the mmWave bands [3], while 6G research is already focusing on the so-called sub-terahertz (THz) bands, i.e., in the range 100–300 GHz. The small wavelength of high-frequency signals makes it practically possible to envision arrays with a very large number of antennas, as never seen before. The advent of large spatially-continuous electromagnetic surfaces interacting with wireless signals pushes even further this vision. From the technological point of view, metamaterials represent appealing candidates toward the creation of software-controlled metasurfaces, which can lead to a viable way of realizing spatially-continuous electromagnetic surfaces [4]. Research in this direction is taking place under the names of Holographic MIMO [5], [6], large intelligent surfaces [7], [8], and reconfigurable intelligent surfaces [9], [10]. All this opens new dimensions and brings new opportunities for communications but also for localization and sensing [11].

A. Motivation and Contribution

A side-effect of using large arrays or surfaces combined with high carrier frequencies is to push the electromagnetic propagation towards the regime in which the wavefront associated to the signal transmitted by the source cannot be approximated by a plane wave. In this regime, also the distance information, not only the angle of arrival can be inferred from it. This concept is not new [12] and it has been widely used to develop signal processing algorithms that exploit the spherical wavefront properties to communicate in low rank propagation channels (e.g., [13], [14], [15]) and to pinpoint the position of the source with high accuracy [8], [16], [17], [18], [19], [20], [21], [22], [23], [24]. In this latter context, the question arises of the ultimate accuracy that can be achieved in localization operations. This is important in order to provide benchmarks for evaluating the performance of actual estimators.

Motivated by the above consideration, in this paper we combine electromagnetic propagation concepts with estimation theory, and compute the Cramér-Rao Bound (CRB) for source localization. In doing so, we consider the three Cartesian components of the electric vector field, observed over a rectangular surface, situated in the Fraunhofer radiation region of the source [25, Ch. 15]. In general, the three Cartesian components depend on

Manuscript received 11 October 2021; revised 27 May 2022 and 16 October 2022; accepted 1 November 2022. Date of publication 14 November 2022; date of current version 30 November 2022. The associate editor coordinating the review of this manuscript and approving it for publication was Dr. Vasanthan Raghavan. The work of Luca Sanguinetti and Antonio A. D'Amico were supported by the Italian Ministry of Education and Research (MIUR) through CrossLab Project (Departments of Excellence). This work was supported by MISTI Global Seed Funds through MIT-Italy Program under the MIT-UNIPI Grant (VIII call). An earlier version of this paper was presented at the 2021 Asilomar Conference on Signals, Systems, and Computers [DOI: 10.1109/IEEECONF53345.2021.9723347]. *(Corresponding author: Antonio A. D'Amico.)*

Antonio A. D'Amico, Andrea de Jesus Torres, and Luca Sanguinetti are with the Dipartimento di Ingegneria dell'Informazione, University of Pisa, 56122 Pisa, Italy (e-mail: a.damico@unipi.it; andrea.dejesustorres@phd.unipi.it; luca.sanguinetti@unipi.it).

Moe Win is with the Wireless Information and Network Sciences Laboratory (WINSLab), Massachusetts Institute of Technology (MIT), Cambridge, MA 02139 USA (e-mail: moewin@mit.edu).

Digital Object Identifier 10.1109/TSP.2022.3222102

the radiation vector [25, Ch. 15], which is in turn determined by the current distribution inside the source. This functional dependence is typically overlooked in *standard* signal processing models used for CRB computations and may lead to estimation algorithms with less accuracy than those based on the complete model. Note that similar considerations can be found in [12] where *standard* models are compared to the so-called *analytic model*, based on electromagnetic theory. Particularly, [12] observes that the former typically ignore the nature of the source whose physical characteristics have a profound impact on the generated electromagnetic fields. We will elaborate further on the differences between what we call analytic model and what we collectively denote as standard models later on, after introducing the necessary mathematical machinery.

The first objective of this paper is to compute and analyze the CRB for the localization of a source on the basis of the analytic model, which stems from first principles of electromagnetic theory. In doing so, we assume that the source is an elementary Hertzian dipole and make use of all the three cartesian components of the electric field for estimating its position. This allows us to derive a fundamental limit to the accuracy of estimators that may possibly exploit the entire electric field. This is what we call *holographic positioning* where the holographic term dates back to the ancient greek and literally means "describe everything" [4]. The concept is often connected with metasurfaces, which are two-dimensional surfaces consisting of arrays of reconfigurable elements of metamaterial. We refer to [26] for a recent survey on the implementation aspects for metasurfaces. The main results of our CRB analysis can be summarized as follows.

- We show how the ultimate estimation accuracy for the localization of a source depends on its orientation. To the best of authors' knowledge, such a dependence has never been pointed out before, and comes from considering the radiation vector in the expression of the received electric field.
- The orientation of the source can be assumed known or unknown to the receiver. A second interesting contribution of this paper is to show that, under practical conditions, the CRB computed assuming that the orientation is unknown coincides with that computed assuming that it is perfectly known. This does not mean that we can ignore the effect of dipole orientation in the estimation process but only that the joint estimation of orientation and position ultimately provides the same localization accuracy as if the orientation were known.
- To gain insights about the impact on the estimation accuracy of different system parameters (such as wavelength, size of the receiving surface), we assume that the dipole is located on the line perpendicular to the surface center. In this case, closed-form expressions can be computed that show that the CRB scales quadratically with the wavelength. This is in line with the results in [8] where a standard model was used. Also, we show that the accuracy in the estimation of some components of the position vector improves unboundedly as the ratio between the size of the receiving surface and its distance from the source increases. This is a new result that cannot be found in prior works.

A second important objective of this paper is to use the CRB analysis to understand whether or not positioning algorithms based on the analytic model can provide gains, compared to those based on standard models. To partially answer this question, we consider a planar array made of Hertzian dipoles (filling the receiving surface) and we analyze the performance of three different maximum-likelihood estimators (MLEs) of the source position, which are derived on the basis of three different models of the electric field. In particular, the first estimator makes use of the analytic model adopted in this paper, the second one is based on the model from [8], and the third one relies on the common planar approximation of the received electromagnetic wave. Numerical results are used to compare the different estimators. It turns out that the estimation accuracy of the MLE based on the analytic model is very close to the theoretical limits provided by the CRB. Moreover, we show that it outperforms the other two estimators as it takes into account the orientation of the transmitting dipole. Finally, we show that the estimation accuracy depends on the source orientation, but not on its a priori knowledge. This is exactly in line with the behavior predicted by the CRB analysis.

Compared to the conference version [1], this paper provides a more detailed derivation and discussion of the electromagnetic vector model and computes the CRBs in both cases, that is, with and without a priori knowledge of the source dipole orientation. Also, it provides all the derivations that were omitted in [1], and analyzes the performance of MLEs based on different electric field models.

B. Paper Outline and Notation

The paper is organized as follows. In Section II, we start from first principles of wave propagation theory and provide the most general form of the electric field, which is then used to compute the CRB for the estimation of the position of the transmitting source. We also briefly describe how simplified models can be obtained from the general form. In Section III, we simplify the analysis by assuming that the transmitting source is an elementary dipole pointing in an arbitrary direction. The CRBs for the estimation of the dipole position are computed for both cases, i.e., with and without a priori knowledge of its orientation. To gain insights into the CRBs, in Section IV we assume that the dipole is located in the central perpendicular line (CPL) and is vertically oriented. Insightful closed-form expressions are provided to quantify the ultimate estimation accuracy. In Section V, we provide some numerical results as a function of system parameters, e.g., distance, array size, carrier frequency. To quantify the impact of the electric field model on the estimation accuracy, in Section VI we analyze the performance of three different MLEs. The first is based on the adopted analytic model while the other two are based on models adopted in the literature. The major conclusions are drawn in Section VII.

The following notation is used throughout the paper. In the $\mathbb{R}^3$ Euclidean space, an arbitrary spatial vector $\mathbf{r}$ is represented as $\mathbf{r} = (\alpha, \beta, \gamma)$, where (α, β, γ) are the *components* of $\mathbf{r}$ along the directions of three given orthonormal vectors $\hat{\mathbf{u}}_1, \hat{\mathbf{u}}_2, \hat{\mathbf{u}}_3$. Equivalently, we write $\mathbf{r} = \alpha\hat{\mathbf{u}}_1 + \beta\hat{\mathbf{u}}_2 + \gamma\hat{\mathbf{u}}_3$. The length of $\mathbf{r}$

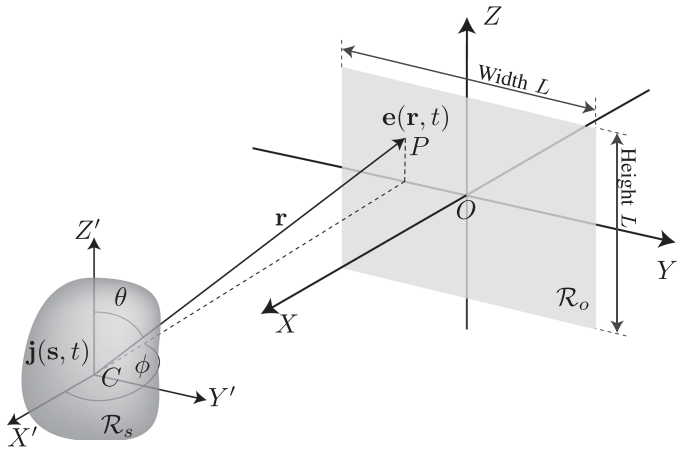

Fig. 1. Geometry of the considered system.

is $||\mathbf{r}|| = \sqrt{\alpha^2+\beta^2+\gamma^2}$, and $\hat{\mathbf{r}} = \mathbf{r}/||\mathbf{r}||$ is a unit vector that is parallel to $\mathbf{r}$. We use $\mathbf{a}\times\mathbf{b}$ and $\mathbf{a}\cdot\mathbf{b}$ to denote, respectively, the cross and the dot product between $\mathbf{a}$ and $\mathbf{b}$. An arbitrary point P in $\mathbb{R}^3$ is described by its three *coordinates* with respect to a reference system (cartesian or spherical). A point P can also be represented by a vector $\mathbf{r}$. In such a case, P is the endpoint of $\mathbf{r}$, whose starting point is fixed.

C. Reproducible Research

The Matlab code used to obtain the simulation results is available at: https://github.com/lucasanguinetti/CRB-for-Holographic-Positioning.

II. Signal Model and Problem Formulation

Consider the system depicted in Fig. 1 in which an electric current density $\mathbf{j}(\mathbf{s},t)$, inside a source region $\mathcal{R}_s$, with $\mathbf{s}$ being a spatial vector identifying a generic point in $\mathcal{R}_s$, generates an electric field $\mathbf{e}(\mathbf{r},t)$ at a generic point P, identified through the spatial vector $\mathbf{r}$. We consider only monochromatic sources and fields of the form

$$\mathbf{j}(\mathbf{s},t) = \text{Re}\left\{\mathbf{j}(\mathbf{s})\mathrm{e}^{\mathrm{j}\omega t}\right\} \tag{1}$$

and

$$\mathbf{e}(\mathbf{r},t) = \text{Re}\left\{\mathbf{e}(\mathbf{r})\mathrm{e}^{\mathrm{j}\omega t}\right\} \tag{2}$$

where ω is frequency in radians/second. In this case, Maxwell's equations can be written only in terms of the current and field *phasors*, $\mathbf{j}(\mathbf{s})$ and $\mathbf{e}(\mathbf{r})$ [27, Ch. 1].

We call C the *centroid* of the source region $\mathcal{R}_s$ and assume that the electric field $\mathbf{e}(\mathbf{r})$, produced by $\mathbf{j}(\mathbf{s})$, is measured over an *observation region* $\mathcal{R}_o$ outside $\mathcal{R}_s$. The electromagnetic field propagates in a homogeneous and isotropic medium with neither obstacles nor reflecting surfaces. In other words, there is only a line-of-sight link between $\mathcal{R}_s$ and $\mathcal{R}_o$.

A. Signal Model

The measured field is the sum of $\mathbf{e}(\mathbf{r})$ and a random noise field $\mathbf{n}(\mathbf{r})$, i.e.,

$$\boldsymbol{\xi}(\mathbf{r}) = \mathbf{e}(\mathbf{r}) + \mathbf{n}(\mathbf{r}) \tag{3}$$

where $\mathbf{n}(\mathbf{r})$ is generated by electromagnetic sources outside $\mathcal{R}_s$. In an unbounded, homogeneous and isotropic medium, the electric field $\mathbf{e}(\mathbf{r})$ can be written as [27, Ch. 1]

$$\mathbf{e}(\mathbf{r}) = -\mathrm{j}kZ_0 \int_{\mathcal{R}_s} \overline{\overline{\mathbf{G}}}(\mathbf{r}-\mathbf{s})\cdot\mathbf{j}(\mathbf{s})\mathrm{d}\mathbf{s} \tag{4}$$

where $k = 2\pi/\lambda$ is the *wavenumber*, $\lambda = 2\pi c/\omega$ is the *wavelength*, Z_0 is the intrinsic impedance of the medium, and $\overline{\overline{\mathbf{G}}}(\mathbf{p})$ is the dyadic Green's function, given by [28]

$$\overline{\overline{\mathbf{G}}}(\mathbf{p}) = g(p)\left[\left(1-\mathrm{j}\frac{1}{kp}-\frac{1}{k^2p^2}\right)\overline{\overline{\mathbf{I}}} - \left(1-\mathrm{j}\frac{3}{kp}-\frac{3}{k^2p^2}\right)\hat{\mathbf{p}}\hat{\mathbf{p}}\right] \tag{5}$$

where $\overline{\overline{\mathbf{I}}}$ is the unit dyad, $p = \|\mathbf{p}\|$, $\hat{\mathbf{p}} = \mathbf{p}/p$, and $g(p)$ is the scalar Green's function, i.e.,

$$g(p) = \frac{e^{-\mathrm{j}kp}}{4\pi p}. \tag{6}$$

Consider a cartesian coordinate system $CX'Y'Z'$ with the origin in the centroid C in Fig. 1, and let $\hat{\mathbf{x}}$, $\hat{\mathbf{y}}$ and $\hat{\mathbf{z}}$, unit vectors in the X', Y' and Z' directions, respectively. We make the following assumption.

Assumption 1 (Fraunhofer radiation region of the source): *Let r_o be the minimum distance of C from $\mathcal{R}_o$ and denote by l_s the largest dimension of $\mathcal{R}_s$. We assume that $r_o \gg l_s$ and $r_o \gg 2l_s^2/\lambda$. These conditions define the so-called far-field or Fraunhofer radiation region of the source [25, Ch. 15].*

Under Assumption 1, the electric field $\mathbf{e}(\mathbf{r})$ can be approximated as [25, Ch. 15]:

$$\mathbf{e}(\mathbf{r}) = G(r)\left[\hat{\mathbf{r}}\times\mathbf{R}(\theta,\phi)\right]\times\hat{\mathbf{r}} \tag{7}$$

where

$$G(r) = -\mathrm{j}kZ_0 g(r) \tag{8}$$

and (r,θ,ϕ) are the spherical coordinates (with respect to $CX'Y'Z'$) of a generic point $\mathbf{r}\in\mathcal{R}_o$, i.e., $\mathbf{r} = r\cos\phi\sin\theta\hat{\mathbf{x}} + r\sin\phi\sin\theta\hat{\mathbf{y}} + r\cos\theta\hat{\mathbf{z}}$. Also, $\hat{\mathbf{r}}$ is the unit vector in the radial direction and $\mathbf{R}(\theta,\phi)$ is the *radiation vector*. This is related to the source current distribution $\mathbf{j}(\mathbf{s})$ as follows [25, Eq. (15.7.5)]

$$\mathbf{R}(\theta,\phi) = \int_{\mathcal{R}_s}\mathbf{j}(\mathbf{s})\mathrm{e}^{\mathrm{j}\mathbf{k}(\theta,\phi)\cdot\mathbf{s}}d\mathbf{s} \tag{9}$$

where $\mathbf{k}(\theta,\phi) = k\hat{\mathbf{r}}$ is the *wavenumber vector*. Denote by $R_r(\theta,\phi)$, $R_\theta(\theta,\phi)$ and $R_\phi(\theta,\phi)$ the components of the radiation vector $\mathbf{R}(\theta,\phi)$ along the $\hat{\mathbf{r}}$, $\hat{\boldsymbol{\theta}}$ and $\hat{\boldsymbol{\phi}}$ directions. Then, we may write:

$$\mathbf{R}(\theta,\phi) = R_r(\theta,\phi)\hat{\mathbf{r}} + R_\theta(\theta,\phi)\hat{\boldsymbol{\theta}} + R_\phi(\theta,\phi)\hat{\boldsymbol{\phi}} \tag{10}$$

where

$$\hat{\mathbf{r}} = \sin\theta\cos\phi\hat{\mathbf{x}} + \sin\theta\sin\phi\hat{\mathbf{y}} + \cos\theta\hat{\mathbf{z}} \tag{11}$$

$$\hat{\boldsymbol{\theta}} = \cos\theta\cos\phi\hat{\mathbf{x}} + \cos\theta\sin\phi\hat{\mathbf{y}} - \sin\theta\hat{\mathbf{z}} \tag{12}$$

$$\hat{\boldsymbol{\phi}} = -\sin\phi\hat{\mathbf{x}} + \cos\phi\hat{\mathbf{y}}. \tag{13}$$

Plugging (10) into (7) yields

$$\mathbf{e}(\mathbf{r}) = G(r)\left[R_\theta(\theta,\phi)\hat{\boldsymbol{\theta}} + R_\phi(\theta,\phi)\hat{\boldsymbol{\phi}}\right] \tag{14}$$

since $\hat{\mathbf{r}} \times \hat{\mathbf{r}} = \mathbf{0}$, $(\hat{\mathbf{r}} \times \hat{\boldsymbol{\theta}}) \times \hat{\mathbf{r}} = \hat{\boldsymbol{\theta}}$ and $(\hat{\mathbf{r}} \times \hat{\boldsymbol{\phi}}) \times \hat{\mathbf{r}} = \hat{\boldsymbol{\phi}}$.[1] Notice that $\mathbf{e}(\mathbf{r})$ in (14) is completely determined by the transverse component

$$\mathbf{R}_{\perp}(\theta, \phi) = R_{\theta}(\theta, \phi)\hat{\boldsymbol{\theta}} + R_{\phi}(\theta, \phi)\hat{\boldsymbol{\phi}} \tag{15}$$

of the radiation vector $\mathbf{R}(\theta, \phi)$ [25, Ch. 15]. Similar to [12], in what follows we refer to (7) as the *analytic* model.

Denote by $\xi_x(\mathbf{r})$, $\xi_y(\mathbf{r})$ and $\xi_z(\mathbf{r})$, the cartesian components of $\boldsymbol{\xi}(\mathbf{r})$ along the $\hat{\mathbf{x}}$, $\hat{\mathbf{y}}$ and $\hat{\mathbf{z}}$ directions, respectively. From (3), we have

$$\xi_x(\mathbf{r}) = [\mathbf{e}(\mathbf{r}) + \mathbf{n}(\mathbf{r})] \cdot \hat{\mathbf{x}} = e_x(\mathbf{r}) + n_x(\mathbf{r}) \tag{16}$$

$$\xi_y(\mathbf{r}) = [\mathbf{e}(\mathbf{r}) + \mathbf{n}(\mathbf{r})] \cdot \hat{\mathbf{y}} = e_y(\mathbf{r}) + n_y(\mathbf{r}) \tag{17}$$

$$\xi_z(\mathbf{r}) = [\mathbf{e}(\mathbf{r}) + \mathbf{n}(\mathbf{r})] \cdot \hat{\mathbf{z}} = e_z(\mathbf{r}) + n_z(\mathbf{r}) \tag{18}$$

where $e_x(\mathbf{r}), e_y(\mathbf{r})$ and $e_z(\mathbf{r})$ are obtained from (14) by using (11)–(13). This yields

$$e_x(\mathbf{r}) = G(r)\left[R_{\theta}(\theta, \phi)\cos\theta\cos\phi - R_{\phi}(\theta, \phi)\sin\phi\right] \tag{19}$$

$$e_y(\mathbf{r}) = G(r)\left[R_{\theta}(\theta, \phi)\cos\theta\sin\phi + R_{\phi}(\theta, \phi)\cos\phi\right] \tag{20}$$

$$e_z(\mathbf{r}) = -G(r)R_{\theta}(\theta, \phi)\sin\theta. \tag{21}$$

B. Problem Formulation

We aim at computing the CRB for the estimation of the position of the centroid C in Fig. 1 based on the noisy vector $\boldsymbol{\xi}(\mathbf{r})$ over the observation region $\mathcal{R}_o$, whose cartesian components are given by (16)–(18). For this purpose, the following assumptions are further made.

Assumption 2: *The observation region is a square domain parallel to the $Y'Z'$ coordinate plane. In particular, assume that*

$$\mathcal{R}_o = \{(x,' y,' z') : x' = x'_o, |y' - y'_o| \le L/2, |z' - z'_o| \le L/2\}$$

where (x'_o, y'_o, z'_o) are the cartesian coordinates of the center O of $\mathcal{R}_o$ in the system $CX'Y'Z'$.

Assumption 3 (Random noise field modelling): *Following [29]–[30], we model $\mathbf{n}(\mathbf{r})$ as a spatially uncorrelated zero-mean complex Gaussian process with correlation function*

$$\mathrm{E}\left\{\mathbf{n}(\mathbf{r})\mathbf{n}^{\dagger}(\mathbf{r}')\right\} = \sigma^2\mathbf{I}\delta(\mathbf{r} - \mathbf{r}') \tag{22}$$

where $\mathbf{I}$ is the identity matrix, $\delta(\cdot)$ is the Dirac's delta function, and σ^2 is measured in V^2, where V indicates volts [30].

The cartesian system $OXYZ$ in Fig. 1 is obtained by $CX'Y'Z'$ through a pure translation. The position of C in the system $OXYZ$ is given by the cartesian coordinates (x_C, y_C, z_C). Accordingly, we have that $x' = x - x_C$, $y' = y - y_C$ and $z' = z - z_C$.

Let $\mathbf{u} = (x_C, y_C, z_C)$ denote the vector collecting the *unknown* coordinates of C. The CRB for the estimation of the ith entry of $\mathbf{u}$, say u_i, is (e.g., [31])

$$\mathrm{CRB}(u_i) = \left[\mathbf{F}^{-1}\right]_{ii} \tag{23}$$

where $\mathbf{F}$ is the Fisher's Information Matrix (FIM). The latter is a 3×3 hermitian matrix, whose elements are computed as [31, Appendix 15C]

$$[\mathbf{F}]_{mn} = \frac{2}{\sigma^2}\mathrm{Re}\left\{\iint_{-\frac{L}{2}}^{\frac{L}{2}} f_{mn}(y, z)dydz\right\} \tag{24}$$

where

$$f_{mn}(y, z) = \frac{\partial e_x(\mathbf{r})}{\partial u_m}\frac{\partial e_x^*(\mathbf{r})}{\partial u_n} + \frac{\partial e_y(\mathbf{r})}{\partial u_m}\frac{\partial e_y^*(\mathbf{r})}{\partial u_n} + \frac{\partial e_z(\mathbf{r})}{\partial u_m}\frac{\partial e_z^*(\mathbf{r})}{\partial u_n} \tag{25}$$

and the integration is performed over the observation region $\mathcal{R}_o$, as defined in Assumption 2. The functional dependence of $e_x(\mathbf{r}), e_y(\mathbf{r})$ and $e_z(\mathbf{r})$ on $\mathbf{u}$ is hidden in the spherical coordinates (r, θ, ϕ). Indeed, we have

$$r = ||\mathbf{r}|| = \sqrt{x_C^2 + (y - y_C)^2 + (z - z_C)^2} \tag{26}$$

$$\cos\theta = \frac{z - z_C}{r} \tag{27}$$

$$\tan\phi = -\frac{y - y_C}{x_C}. \tag{28}$$

Accordingly, we can write

$$\frac{\partial e_v(\mathbf{r})}{\partial u_i} = \frac{\partial e_v(\mathbf{r})}{\partial r}\frac{\partial r}{\partial u_i} + \frac{\partial e_v(\mathbf{r})}{\partial \theta}\frac{\partial \theta}{\partial u_i} + \frac{\partial e_v(\mathbf{r})}{\partial \phi}\frac{\partial \phi}{\partial u_i} \tag{29}$$

with $v \in \{x, y, z\}$ and $i \in \{1, 2, 3\}$. The derivatives of r, θ and ϕ with respect to u_i can be easily computed from (26)–(28), whereas the partial derivatives of $e_v(\mathbf{r})$ with respect to r, θ and ϕ can be obtained from (19)–(21).

It is clear that the computation of (29) requires knowledge of the components $R_{\theta}(\theta, \phi)$ and $R_{\phi}(\theta, \phi)$ of the radiation vector $\mathbf{R}(\theta, \phi)$. In other words, the evaluation of (29) implicitly assumes that the current distribution inside the source region $\mathcal{R}_s$ is a priori known. However, this is not always the case in practical applications. When it is *not* a priori known, the problem must be reformulated to take into account this lack of information. In the remainder of this paper, we consider a specific scenario in which the current source is an elementary (i.e., short) dipole with an arbitrary orientation and address the estimation problem in both cases, that is, *with* and *without* a priori knowledge of the current distribution.

C. Discussion on Prior Adopted Electromagnetic Models

The expression in (14) provides the electric field $\mathbf{e}(\mathbf{r})$ in a point $\mathbf{r}$ lying in the Fraunhofer radiation region of the source (i.e., under Assumption 1). We see that $\mathbf{e}(\mathbf{r})$ is the product of the two terms: $G(r)$ and $\mathbf{R}_{\perp}(\theta, \phi) = R_{\theta}(\theta, \phi)\hat{\boldsymbol{\theta}} + R_{\phi}(\theta, \phi)\hat{\boldsymbol{\phi}}$. The first term is given in (8) and represents a scalar spherical wave, which accounts for the distance r between the source and the point, as given in (26). The second term is defined in (15) and takes into account the vector nature of $\mathbf{e}(\mathbf{r})$ as well as its *dependence on the current distribution inside the transmitting volume*. In general, such a dependence is overlooked in the literature. To the best of our knowledge, [12] is the only paper in which it is recognized that the commonly adopted models do not consider the characteristics of the source (transmit antenna type, size, orientation, etc.), although it may significantly affect the structure of the received electric field. In general, the standard

[1] Notice that $\hat{\mathbf{r}} \times \hat{\boldsymbol{\theta}} = -\hat{\boldsymbol{\phi}}$, $-\hat{\boldsymbol{\phi}} \times \hat{\mathbf{r}} = \hat{\boldsymbol{\theta}}$, $\hat{\mathbf{r}} \times \hat{\boldsymbol{\phi}} = -\hat{\boldsymbol{\theta}}$ and $-\hat{\boldsymbol{\theta}} \times \hat{\mathbf{r}} = \hat{\boldsymbol{\phi}}$.

models for CRB computation and position estimation have the following form [12]:

$$\eta(\mathbf{r}) = s(\mathbf{r}) + n(\mathbf{r}) \tag{30}$$

where

$$s(\mathbf{r}) = f(\mathbf{e}(\mathbf{r})) \tag{31}$$

is some *scalar* function $f(\cdot)$ of the received electric field and $n(\mathbf{r})$ is additive noise. The vast majority of models is obtained as a further simplification of (30) in which only the spherical wave term $G(r)$ is considered, e.g., [24]. This leads to:

$$s(\mathbf{r}) = \alpha G(r) \tag{32}$$

where α is a scaling parameter independent of the observation point. The analyses provided in [17], [18], and [21], are based on the above model. A more accurate scalar model is considered in [8]. Here, the authors assume that the received signal can be written as [8, Eq. (2)]

$$s(\mathbf{r}) = \beta G(r)\sqrt{\frac{x_C}{r}} \tag{33}$$

where the additional factor $\sqrt{x_C/r}$ accounts for the angle-of-arrival of the transmitted signal. The same model is adopted in [16].

D. The Planar Wave Approximation

In the region $\mathcal{R}_o$, we have that $\mathbf{r} = \mathbf{r}_C + \mathbf{d}$, where $\mathbf{r}_C = -x_C\hat{\mathbf{x}} + y_C\hat{\mathbf{y}} + z_C\hat{\mathbf{z}}$ is the vector from C to O and $\mathbf{d} = y\hat{\mathbf{y}} + z\hat{\mathbf{z}}$ is the vector from O to P. Accordingly, (26) reduces to

$$r = \|\mathbf{r}_C + \mathbf{d}\| = r_C\sqrt{1 + 2(\hat{\mathbf{r}}_C \cdot \hat{\mathbf{d}})\frac{d}{r_C} + \frac{d^2}{r_C^2}} \tag{34}$$

with $r_C = \|\mathbf{r}_C\|$ and $d = \|\mathbf{d}\|$. In the case $r_C \gg d$, we can replace r with r_C in the denominator of (6) and obtain the following approximation:

$$G(r) \approx -\mathrm{j}kZ_0\frac{\mathrm{e}^{-\mathrm{j}kr}}{4\pi r_C}. \tag{35}$$

As for the exponent $\mathrm{e}^{-\mathrm{j}kr}$, approximations may be obtained by considering the Taylor series expansion $\sqrt{1+x} \approx 1 + x/2 - x^2/8$, valid for small values of x. Applying this approximation to (34) yields

$$r \approx r_C + (\hat{\mathbf{r}}_C \cdot \hat{\mathbf{d}})d + [1 - (\hat{\mathbf{r}}_C \cdot \hat{\mathbf{d}})^2]d^2/2r_C \tag{36}$$

and (35) thus reduces to

$$G(r) \approx -\mathrm{j}kZ_0\frac{\mathrm{e}^{-\mathrm{j}kr_C}}{4\pi r_C}\mathrm{e}^{-\mathrm{j}k[d\cos\psi + \sin^2\psi(d^2/2r_C)]} \tag{37}$$

where $\cos\psi = (\hat{\mathbf{r}}_C \cdot \hat{\mathbf{d}})$. This expansion is called the *Fresnel approximation* [12]. In the case $r_C \gg L^2/\lambda$, we can retain only the first-order term in the exponent of (37) and thus obtain

$$G(r) \approx -\mathrm{j}kZ_0\frac{\mathrm{e}^{-\mathrm{j}kr_C}}{4\pi r_C}\mathrm{e}^{-\mathrm{j}kd\cos\psi} \tag{38}$$

which represents the well-known *planar* approximation of the spherical wave in (8).

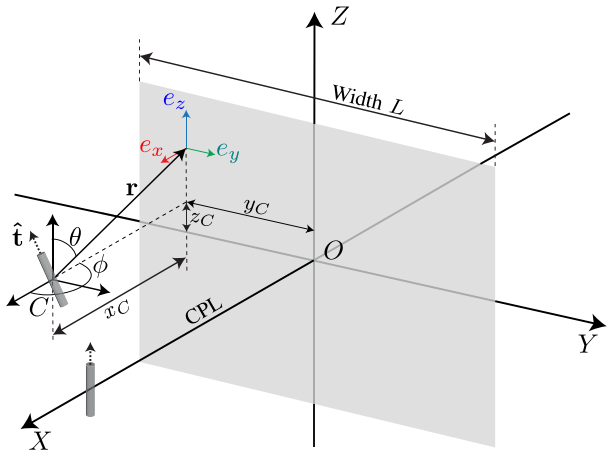

Fig. 2. Illustration of an elementary dipole pointing in an arbitrary direction $\hat{\mathbf{t}} = t_x\hat{\mathbf{x}} + t_y\hat{\mathbf{y}} + t_z\hat{\mathbf{z}}$. The centroid of the dipole has cartesian coordinates (x_C, y_C, z_C). The CPL case in which the dipole is located in the central perpendicular line (CPL) and is vertically oriented is also reported.

III. CRB Computation With an Elementary Source Dipole

To simplify the analysis, we make the following assumption about the source, as shown in Fig. 2.

Assumption 4: *The source is an elementary dipole of length l_s pointing in an arbitrary direction $\hat{\mathbf{t}} = t_x\hat{\mathbf{x}} + t_y\hat{\mathbf{y}} + t_z\hat{\mathbf{z}}$.*

In the case of an elementary dipole, the current density $\mathbf{j}(\mathbf{s})$ has the following expression (e.g., [27, Sec. 2.3.1])

$$\mathbf{j}(\mathbf{s}) = I_{in}l_s\delta(\mathbf{s})\hat{\mathbf{t}} \tag{39}$$

where I_{in} is the uniform current level in the dipole. Plugging (39) into (9) yields

$$\mathbf{R}(\theta, \phi) = I_{in}l_s\hat{\mathbf{t}} \tag{40}$$

from which, using (7), we have

$$\mathbf{e}(\mathbf{r}) = G(r)I_{in}l_s[(\hat{\mathbf{r}}\times\hat{\mathbf{t}}) \times\hat{\mathbf{r}}]. \tag{41}$$

By using the identity $(\hat{\mathbf{r}} \times \hat{\mathbf{t}})\times\hat{\mathbf{r}} = \hat{\mathbf{t}} - (\hat{\mathbf{r}} \cdot \hat{\mathbf{t}})\hat{\mathbf{r}}$, (41) can be written in the equivalent form

$$\mathbf{e}(\mathbf{r}) = G(r)I_{in}l_s[\hat{\mathbf{t}} - (\hat{\mathbf{r}} \cdot \hat{\mathbf{t}})\hat{\mathbf{r}}]. \tag{42}$$

From (8) and (42), it thus follows that

$$e_x = -\mathrm{j}\chi\frac{\mathrm{e}^{-\mathrm{j}kr}}{r}[t_x - (r_xt_x + r_yt_y + r_zt_z)r_x] \tag{43}$$

$$e_y = -\mathrm{j}\chi\frac{\mathrm{e}^{-\mathrm{j}kr}}{r}[t_y - (r_xt_x + r_yt_y + r_zt_z)r_y] \tag{44}$$

$$e_z = -\mathrm{j}\chi\frac{\mathrm{e}^{-\mathrm{j}kr}}{r}[t_z - (r_xt_x + r_yt_y + r_zt_z)r_z] \tag{45}$$

where (r_x, r_y, r_z) are the cartesian components of $\hat{\mathbf{r}}$, and

$$\chi = \frac{Z_0I_{in}}{2}\frac{l_s}{\lambda} \tag{46}$$

is measured in volts, V. For the sake of simplicity, we have dropped the dependence of e_x, e_y and e_z on $\mathbf{r}$. The above expressions depend on (t_x, t_y, t_z) and the cartesian coordinates

(x_C, y_C, z_C) of the centroid C, which are related to (r_x, r_y, r_z) through the following equations:

$$r_x = -\frac{x_C}{r}, \quad r_y = \frac{y - y_C}{r}, \quad r_z = \frac{z - z_C}{r} \tag{47}$$

where r is given by (26).

We aim at evaluating the CRBs for the estimation of (x_C, y_C, z_C) on the basis of (43)–(45). We first consider the case in which the parameters (t_x, t_y, t_z) are *unknown* and thus must be considered as *nuisance* parameters. This corresponds to the case of having *partial* information about the source current distribution. This first case is not only more general but also instrumental to obtain the CRBs with *full* information, i.e., the parameters (t_x, t_y, t_z) are a priori *known*.

A. Unknown Orientation of the Dipole

When (t_x, t_y, t_z) are unknown, we cannot use (23)–(25) but we must compute the FIM for *all* the unknown parameters, which are collected into the 6-dimensional vector $\mathbf{p} = (t_x, t_y, t_z, x_C, y_C, z_C)$. Therefore, the FIM is a 6×6 symmetric matrix with entries given by

$$[\mathbf{F}]_{mn} = \frac{2}{\sigma^2}\mathrm{Re}\left\{ \iint_{-\frac{L}{2}}^{\frac{L}{2}} \left[\frac{\partial e_x}{\partial p_m}\frac{\partial e_x^*}{\partial p_n} + \frac{\partial e_y}{\partial p_m}\frac{\partial e_y^*}{\partial p_n} + \frac{\partial e_z}{\partial p_m}\frac{\partial e_z^*}{\partial p_n} \right] dydz \right\} \tag{48}$$

where p_m denotes the mth element of $\mathbf{p}$ and $\mathrm{Re}\{\cdot\}$ is the real part of the enclosed quantity. The derivatives involved in $[\mathbf{F}]_{mn}$ are computed in Appendix A. The matrix $\mathbf{F}$ can be partitioned as [31]

$$\mathbf{F} = \left[\begin{array}{c|c} \mathbf{F}_{tt} & \mathbf{F}_{tc} \\ \hline \mathbf{F}_{ct} & \mathbf{F}_{cc} \end{array}\right] \tag{49}$$

where the 3×3 blocks $\mathbf{F}_{tt}$ and $\mathbf{F}_{cc}$ contain the partial derivatives with respect to (t_x, t_y, t_z) and (x_C, y_C, z_C), respectively, while $\mathbf{F}_{tc}$ and $\mathbf{F}_{ct}$ contain the mixed derivatives. Since $\mathbf{F}$ is symmetric, we have $\mathbf{F}_{tt} = \mathbf{F}_{tt}^T$, $\mathbf{F}_{cc} = \mathbf{F}_{cc}^T$ and $\mathbf{F}_{tc} = \mathbf{F}_{ct}^T$. Based on (49) and well known formulas on the inverse of partitioned matrices [31, Sec. A1.1.3], we can immediately show that the CRBs for the estimation of x_C, y_C and z_C, are given by the diagonal elements of the matrix $(\mathbf{F}_{cc} - \mathbf{F}_{tc}^T\mathbf{F}_{tt}^{-1}\mathbf{F}_{tc})^{-1}$, i.e.,

$$\mathrm{CRB}_{\mathrm{u}}(x_C) = \left[\left(\mathbf{F}_{cc} - \mathbf{F}_{tc}^T\mathbf{F}_{tt}^{-1}\mathbf{F}_{tc}\right)^{-1}\right]_{11} \tag{50}$$

$$\mathrm{CRB}_{\mathrm{u}}(y_C) = \left[\left(\mathbf{F}_{cc} - \mathbf{F}_{tc}^T\mathbf{F}_{tt}^{-1}\mathbf{F}_{tc}\right)^{-1}\right]_{22} \tag{51}$$

$$\mathrm{CRB}_{\mathrm{u}}(z_C) = \left[\left(\mathbf{F}_{cc} - \mathbf{F}_{tc}^T\mathbf{F}_{tt}^{-1}\mathbf{F}_{tc}\right)^{-1}\right]_{33} \tag{52}$$

where the subscript $_{\mathrm{u}}$ is used to stress that the above results refer to the case of *unknown* dipole orientation.

Remark 1: *Notice that the electromagnetic model in (43)–(45) can also be used to compute the CRBs for the cartesian components (t_x, t_y, t_z) of $\hat{\mathbf{t}}$. Evaluating these bounds is out of the scope of this work whose focus is the estimation of the source position. However, we point out that estimating the orientation may be useful in practice, e.g., for the deployment and orientation of receiving surfaces.*

B. Known Orientation of Dipole

When the arbitrary parameters (t_x, t_y, t_z) of the dipole are perfectly known, we have a complete description of the source current distribution. This means that the functions $R_\theta(\theta, \phi)$ and $R_\phi(\theta, \phi)$ are known, and we can compute the CRB following the general[2] procedure outlined in Section II-B. The Fisher's information matrix obtained in this way coincides with the matrix $\mathbf{F}_{cc}$ computed previously. It thus follows that the CRBs for the estimation of x_C, y_C and z_C, can be found as the diagonal elements of the matrix $\mathbf{F}_{cc}^{-1}$, i.e.,

$$\mathrm{CRB}(x_C) = \left[\mathbf{F}_{cc}^{-1}\right]_{11} \tag{53}$$

$$\mathrm{CRB}(y_C) = \left[\mathbf{F}_{cc}^{-1}\right]_{22} \tag{54}$$

$$\mathrm{CRB}(z_C) = \left[\mathbf{F}_{cc}^{-1}\right]_{33}. \tag{55}$$

C. Relationship Between CRBs With and Without Knowledge of the Dipole Orientation

By applying the matrix inversion lemma,[3] we obtain

$$\left[\left(\mathbf{F}_{cc} - \mathbf{F}_{tc}^T\mathbf{F}_{tt}^{-1}\mathbf{F}_{tc}\right)^{-1}\right]_{ii} = \left[\mathbf{F}_{cc}^{-1}\right]_{ii} + \left[\mathbf{F}_{cc}^{-1}\mathbf{F}_{tc}^T\left(\mathbf{F}_{tt} - \mathbf{F}_{tc}\mathbf{F}_{cc}^{-1}\mathbf{F}_{tc}^T\right)^{-1}\mathbf{F}_{tc}\mathbf{F}_{cc}^{-1}\right]_{ii} \tag{56}$$

for $i = 1, 2, 3$. Notice that $(\mathbf{F}_{tt} - \mathbf{F}_{tc}\mathbf{F}_{cc}^{-1}\mathbf{F}_{tc}^T)^{-1}$ is positive semi-definite, since it is the 3×3 block in the upper left corner of the semi-positive definite matrix $\mathbf{F}^{-1}$. As a result, the second matrix $\mathbf{F}_{cc}^{-1}\mathbf{F}_{tc}^T(\mathbf{F}_{tt} - \mathbf{F}_{tc}\mathbf{F}_{cc}^{-1}\mathbf{F}_{tc}^T)^{-1}\mathbf{F}_{tc}\mathbf{F}_{cc}^{-1}$ in (56) is positive semi-definite as well. Hence, from (56) it follows that

$$\left[\mathbf{F}_{cc}^{-1}\right]_{ii} \leq \left[\left(\mathbf{F}_{cc} - \mathbf{F}_{tc}^T\mathbf{F}_{tt}^{-1}\mathbf{F}_{tc}\right)^{-1}\right]_{ii}. \tag{57}$$

By exploiting this result, we have that

$$\mathrm{CRB}(x_C) \leq \mathrm{CRB}_{\mathrm{u}}(x_C) \tag{58}$$

$$\mathrm{CRB}(y_C) \leq \mathrm{CRB}_{\mathrm{u}}(y_C) \tag{59}$$

$$\mathrm{CRB}(z_C) \leq \mathrm{CRB}_{\mathrm{u}}(z_C) \tag{60}$$

as it should be since the Cramér-Rao bound worsens in the presence of unknown nuisance parameters [31, Example 3.7]. However, numerical results will show that the loss in estimation accuracy between the two cases in which the parameters (t_x, t_y, t_z) are unknown and known may be negligible under certain conditions. More details will be given in Section V.

IV. A Case Study

The elements of the matrices needed for the computation of $\mathbf{F}$ in (49) can be obtained by numerically evaluating the integrals (48) for any arbitrary position of the dipole. Although possible, this makes it hard to gain insights into the CRBs. Next, we show that closed-form expressions can be obtained when the dipole is located in the central perpendicular line (CPL) and is

[2]Here, by *general* we mean that it is valid irrespective of the particular current distribution, as long as the latter is known.

[3]$(\mathbf{A} + \mathbf{UCV})^{-1} = \mathbf{A}^{-1} - \mathbf{A}^{-1}\mathbf{U}(\mathbf{C}^{-1} + \mathbf{VA}^{-1}\mathbf{U})^{-1}\mathbf{VA}^{-1}$

vertically oriented; see Fig. 2. The following assumption is thus made.

Assumption 5: *The center C of the dipole is on the line perpendicular to $\mathcal{R}_o$ passing through the point O (known as CPL case), as shown in Fig. 2, and the dipole is vertically oriented.*

Under the CPL assumption, we have that $y_C = z_C = 0$, whereas the vertical orientation of the dipole implies that $t_x = t_y = 0$ and $t_z = 1$. For convenience, we call

$$\text{SNR} \triangleq \frac{2|\chi|^2}{\sigma^2} \tag{61}$$

the signal-to-noise ratio (SNR) with χ given by (46) and define

$$\rho \triangleq \frac{L}{x_C}. \tag{62}$$

The following result is obtained.

Proposition 1: *Under Assumption 5, we have that:*

1) The matrix $\mathbf{F}_{cc}$ becomes diagonal with entries

$$[\mathbf{F}_{cc}]_{11} = \text{SNR} \cdot \left[k^2 \mathcal{I}_1(\rho) + x_C^{-2} \mathcal{I}_2(\rho)\right] \tag{63}$$

$$[\mathbf{F}_{cc}]_{22} = \text{SNR} \cdot \left[k^2 \mathcal{I}_3(\rho) + x_C^{-2} \mathcal{I}_4(\rho)\right] \tag{64}$$

$$[\mathbf{F}_{cc}]_{33} = \text{SNR} \cdot \left[k^2 \mathcal{I}_5(\rho) + x_C^{-2} \mathcal{I}_6(\rho)\right] \tag{65}$$

where $\mathcal{I}_i(\rho)$ for $i = 1, \ldots, 6$ are given in Appendix B.

2) The matrix $\mathbf{F}_{tt}$ becomes diagonal with entries

$$[\mathbf{F}_{tt}]_{11} = \text{SNR} \cdot \mathcal{I}_7(\rho) \tag{66}$$

$$[\mathbf{F}_{tt}]_{22} = [\mathbf{F}_{tt}]_{33} = \text{SNR} \cdot \mathcal{I}_8(\rho) \tag{67}$$

where $\mathcal{I}_i(\rho)$ for $i = 7, 8$ are given in (108)–(109) in Appendix B.

3) The elements of $\mathbf{F}_{tc}$ are all zero except for $[\mathbf{F}_{tc}]_{13}$ and $[\mathbf{F}_{tc}]_{31}$ which can be computed as

$$[\mathbf{F}_{tc}]_{13} = x_C^{-1} \text{SNR} \cdot \mathcal{I}_9(\rho) \tag{68}$$

$$[\mathbf{F}_{tc}]_{31} = -x_C^{-1} \text{SNR} \cdot \mathcal{I}_{10}(\rho) \tag{69}$$

where $\mathcal{I}_9(\rho)$ and $\mathcal{I}_{10}(\rho)$ are given, respectively, by (112) and (113) in Appendix B.

Proof: The proof is given in Appendix B.

Based on the results in Proposition 1, the following corollaries are obtained for both cases with unknown and known dipole orientation. Notice that the dependence on ρ is omitted to simplify the notation.

Corollary 1 (Unknown dipole orientation): *Under Assumption 5, the CRBs for the estimation of x_C, y_C and z_C when the dipole orientation is unknown are given by*

$$\text{CRB}_\text{u}(x_C) = \frac{\text{SNR}^{-1}}{k^2 \mathcal{I}_1 + x_C^{-2}(\mathcal{I}_2 - \mathcal{I}_8^{-1} \mathcal{I}_{10}^2)} \tag{70}$$

$$\text{CRB}_\text{u}(y_C) = \frac{\text{SNR}^{-1}}{k^2 \mathcal{I}_3 + x_C^{-2} \mathcal{I}_4} \tag{71}$$

$$\text{CRB}_\text{u}(z_C) = \frac{\text{SNR}^{-1}}{k^2 \mathcal{I}_5 + x_C^{-2}(\mathcal{I}_6 - \mathcal{I}_7^{-1} \mathcal{I}_9^2)}. \tag{72}$$

Proof: The proof follows from (50)–(52) by using the results of Proposition 1 from which we have $\mathbf{F}_{tc}^T \mathbf{F}_{tt}^{-1} \mathbf{F}_{tc} = \text{diag}([\mathbf{F}_{tc}]_{31}^2 / [\mathbf{F}_{tt}]_{33}, 0, [\mathbf{F}_{tc}]_{13}^2 / [\mathbf{F}_{tt}]_{11})$.

Corollary 2 (Known dipole orientation): *Under Assumption 5, the CRBs for the estimation of x_C, y_C and z_C when the dipole orientation is known are:*

$$\text{CRB}(x_C) = \frac{\text{SNR}^{-1}}{k^2 \mathcal{I}_1 + x_C^{-2} \mathcal{I}_2} \tag{73}$$

$$\text{CRB}(y_C) = \frac{\text{SNR}^{-1}}{k^2 \mathcal{I}_3 + x_C^{-2} \mathcal{I}_4} \tag{74}$$

$$\text{CRB}(z_C) = \frac{\text{SNR}^{-1}}{k^2 \mathcal{I}_5 + x_C^{-2} \mathcal{I}_6}. \tag{75}$$

Proof: It easily follows from Proposition 1 by using (53)–(55).

The above corollaries clearly show the effects of the wavelength $\lambda = 2\pi/k$ and x_C for fixed values of ρ or, equivalently, of the functions $\{\mathcal{I}_i\}$. Particularly, we see that the estimation accuracy increases as λ or x_C decrease for fixed values of SNR. Similar results were already observed in [8]. Also, from (71) and (74) it follows that, under Assumption 5, $\text{CRB}_\text{u}(y_C) = \text{CRB}(y_C)$.

A. Analysis for $x_C \gg \lambda$

Assumption 5 leads to a considerable simplification since the matrices $\mathbf{F}_{cc}$ and $\mathbf{F}_{tc}^T \mathbf{F}_{tt}^{-1} \mathbf{F}_{tc}$ become diagonal. Further simplifications can be obtained when $x_C \gg \lambda$. This condition is always satisfied in systems operating at frequencies in the range of GHz or above.

Proposition 2: *Under Assumption 5 and $x_C \gg \lambda$, CRBs reduce to*

$$\text{CRB}_\text{u}(x_C) \approx \text{CRB}(x_C) \approx \frac{\text{SNR}^{-1}}{\mathcal{I}_1} \cdot \frac{\lambda^2}{4\pi^2} \tag{76}$$

$$\text{CRB}_\text{u}(y_C) = \text{CRB}(y_C) \approx \frac{\text{SNR}^{-1}}{\mathcal{I}_3} \cdot \frac{\lambda^2}{4\pi^2} \tag{77}$$

Proof: See Appendix C.

Proposition 2 shows that, when $x_C \gg \lambda$, the accuracy in the estimation of x_C and y_C solely depends on the values of λ and ρ. In particular, keeping ρ fixed, the CRBs for x_C and y_C scale with the square of λ. On the other hand, for a given value of λ, if x_C increases by a factor α, we must scale L by the same factor in order to keep ρ, and hence the estimation accuracy, unchanged. This means that the area of the observation region must be increased by a factor α^2. The same conclusions do not hold for the estimation of z_C. Indeed, under Assumption 5 and $x_C \gg \lambda$ it can be shown that the terms $x_C^{-2}(\mathcal{I}_6 - \mathcal{I}_7^{-1} \mathcal{I}_9^2)$ and $x_C^{-2} \mathcal{I}_6$, appearing in the denominator of the expressions for $\text{CRB}_u(z_C)$ and $\text{CRB}(z_C)$ in Corollaries 1 and 2, are not negligible with respect to $k^2 \mathcal{I}_5$. Hence, the CRBs cannot be simplified and continue to depend on both x_C and λ.

B. Asymptotic Analysis for $\rho \to \infty$

Starting from the results given above, in order to understand the ultimate performance and to obtain insightful closed form expressions, it is useful to analyze the behaviour of the CRBs in the asymptotic regime $\rho = L/x_C \to \infty$. The main results are summarized in the following proposition.

Proposition 3: *Under Assumption 5 and $x_C \gg \lambda$, in the asymptotic regime $\rho \to \infty$ we have*

$$\lim_{\rho\to\infty} \mathrm{CRB_u}(x_C) = \lim_{\rho\to\infty} \mathrm{CRB}(x_C) = \frac{\mathrm{SNR}^{-1}}{3\pi^3}\lambda^2 \tag{78}$$

$$\lim_{\rho\to\infty} \mathrm{CRB_u}(y_C)\ln\rho = \lim_{\rho\to\infty} \mathrm{CRB}(y_C)\ln\rho = \frac{\mathrm{SNR}^{-1}}{3\pi^3}\lambda^2 \tag{79}$$

$$\lim_{\rho\to\infty} \mathrm{CRB_u}(z_C)\ln\rho = \lim_{\rho\to\infty} \mathrm{CRB}(z_C)\ln\rho = \frac{\mathrm{SNR}^{-1}}{\pi^3}\lambda^2. \tag{80}$$

Proof: See Appendix D.

Proposition 3 shows that, for sufficiently large values of $\rho = L/x_C$, the estimation accuracy is the same in both cases of unknown or known dipole orientation. This means that, even though $\hat{\mathbf{t}}$ is unknown, we can achieve the same accuracy in the estimation of the source position as in the case of known dipole orientation. Clearly, this requires in general the *joint* estimation of $\hat{\mathbf{t}}$ and (x_C, y_C, z_C). It is interesting to note that the CRBs for the estimation of y_C and z_C goes to zero as ρ increases unboundedly. This is in contrast to the results in [8, Eq. (26)] where it is shown that the asymptotic CRBs are identical for all the three dimensions and depend solely on the wavelength λ. This difference is a direct consequence of the different radiation and signal models used for the computation of CRBs. Indeed, in [8] the bounds are derived on the basis of the scalar field (33).

V. Numerical Analysis of Cramér-Rao Bounds

The effect of the various system parameters on the estimation accuracy is now analyzed by numerically evaluating the CRBs according to the general expressions given in (50)–(52) or in (53)–(55) for the unknown or known dipole orientation cases, respectively. We assume that the dipole is located at a distance $x_C = 6$ m, the signal-to-noise ratio is $\mathrm{SNR} = |\chi|^2/\sigma^2 = 10$ dB, and the wavelength is $\lambda = 0.01$ m (corresponding to $f_c = 30$ GHz), unless otherwise specified. When needed to validate the asymptotic analysis, numerical results are given for surfaces of extremely large side length, e.g., up to $L = 10^3$ m. Clearly, this does not mean that we advocate the use of such *practically infinite* surfaces. Indeed, most of the conclusions and insights will be given for values in the range $1\,\mathrm{m} \le L \le 10\,\mathrm{m}$.

A. Analysis for the CPL Case

Fig. 3 shows the square root of the CRB (RCRB), measured in meters [m], for the three components x_C, y_C and z_C, as a function of the surface side length L, for a vertically oriented dipole located in CPL, i.e., under the hypotheses of Assumption 5. Both cases of unknown and known orientation are considered in Fig. 3(a) and Fig. 3(b), respectively. We see that all the RCRBs decrease fast with the surface side length, at least for values of L of practical interest, i.e. in the range $1\,\mathrm{m} \le L \le 10\,\mathrm{m}$. The results in Fig. 3(a) and Fig. 3(b) show that, for a vertically oriented dipole in CPL, the estimation accuracy is virtually the same with both known and unknown orientation - see also Fig. 4. We see that $\mathrm{RCRB}(x_C)$ is much lower than $\mathrm{RCRB}(y_C)$ and $\mathrm{RCRB}(z_C)$ in the range $1\,\mathrm{m} \le L \le 10\,\mathrm{m}$, and the asymptotic limit is achieved for $L \approx 20$ m. Also, as predicted by (79) and (80), $\mathrm{RCRB}(y_C)$ and $\mathrm{RCRB}(z_C)$ decrease unboundedly as L increases. Notice that an accuracy on the order of tens of centimeters in all the three dimensions (as required for example in future automotive and industrial applications, e.g., [32]) is achieved only for $L \approx 3\,\mathrm{m}$, both with known or unknown orientation.

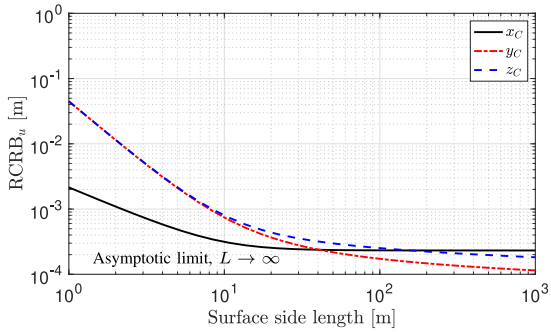

(a) Unknown dipole orientation

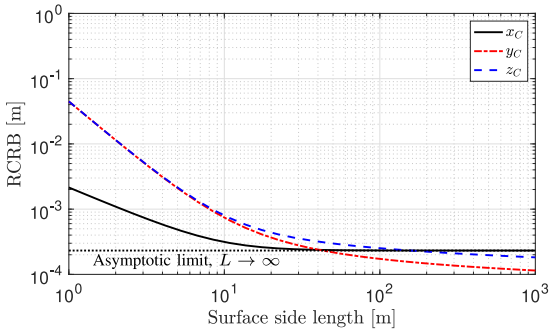

(b) Known dipole orientation

Fig. 3. RCRBs as a function of the surface side length for a vertically oriented dipole in CPL at a distance $x_C = 6$ m.

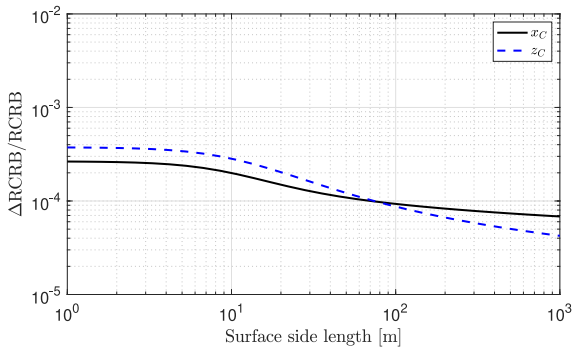

Fig. 4. Loss due to the lack of knowledge of dipole orientation.

To quantify the difference between the CRBs with and without knowledge of dipole orientation, Fig. 4 plots the quantity

$$\left[\frac{\Delta\mathrm{RCRB}}{\mathrm{RCRB}}\right]_{ii} \triangleq \sqrt{\frac{\left[\left(\mathbf{F}_{cc} - \mathbf{F}_{tc}^T\mathbf{F}_{tt}^{-1}\mathbf{F}_{tc}\right)^{-1}\right]_{ii} - [\mathbf{F}_{cc}^{-1}]_{ii}}{[\mathbf{F}_{cc}^{-1}]_{ii}}} \tag{81}$$

as obtained from (56). Notice that y_C is not reported as it is below the numerical precision of Matlab, as expected from the fact that, under Assumption 5, $\mathrm{CRB_u}(y_C) = \mathrm{CRB}(y_C)$. We see that the loss, due to the lack of knowledge of dipole orientation, is negligible for all the considered values of L. This conclusion does not hold true in general. In fact, the role of the dipole

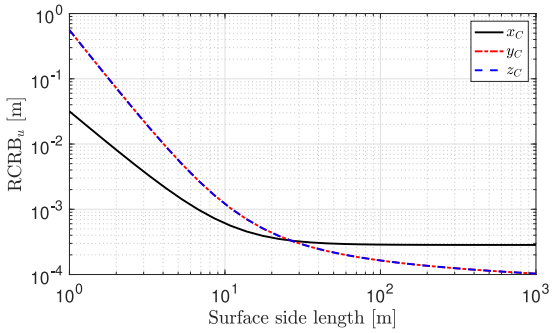

(a) Unknown dipole orientation, $\hat{\mathbf{t}} = (1, 0, 0)$

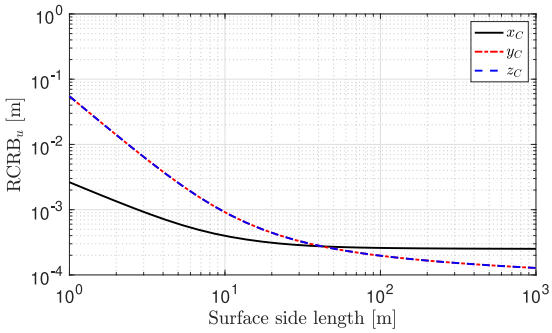

(b) Unknown dipole orientation, $\hat{\mathbf{t}} = (1, 1, 1)/\sqrt{3}$

Fig. 5. RCRBs as a function of the surface side length for two different (unknown) dipole orientations.

orientation in position estimation depends on the operating conditions, and should be verified on a case-by-case basis. In general, having or not knowledge of the dipole orientation has a negligible impact when one of the two (or both) conditions is satisfied: 1) the orientation is well estimated; 2) there is a weak interaction between orientation and position parameters, i.e., the FIM has a nearly block-diagonal structure. In the simulation setting of Figs. 3 and 4, the negligible impact is mainly due to a weak interaction between them.

B. Impact of Dipole Orientation

To quantify the impact of dipole orientation, Fig. 5(a) and Fig. 5(b) show the RCRBs for two different values of $\hat{\mathbf{t}}$, namely $\hat{\mathbf{t}} = (1, 0, 0)$ and $\hat{\mathbf{t}} = (1/\sqrt{3}, 1/\sqrt{3}, 1/\sqrt{3})$. In both cases, the dipole is in CPL and its orientation is unknown. Compared to Fig. 3(a), a sensible loss is evident only when $\hat{\mathbf{t}} = (1, 0, 0)$ and for small values of L. For example, with $L = 3$ m the accuracy in the estimation of x_C decreases from 10 cm to 1 m. Notice that, for both $\hat{\mathbf{t}} = (1, 0, 0)$ and $\hat{\mathbf{t}} = (1/\sqrt{3}, 1/\sqrt{3}, 1/\sqrt{3})$, the accuracy in the estimation of y_C and z_C is the same. Similar conclusions hold when the dipole orientation is known.

Fig. 6 shows the RCRBs in the case of unknown orientation, respectively, as a function of y_C and z_C when $x_C = 6$ m. The dipole is oriented vertically and $L = 3$ m. The value of the RCRB corresponding to a point (y_C, z_C) is measured by the color of that point. More precisely, the RCRB values are first normalized to their minimum, which is achieved when the dipole is in CPL ($y_C = z_C = 0$), and then the normalized values (in dB) are mapped into a colour: higher values are associated to warm colours, lower values to cool ones. This means, for example, that

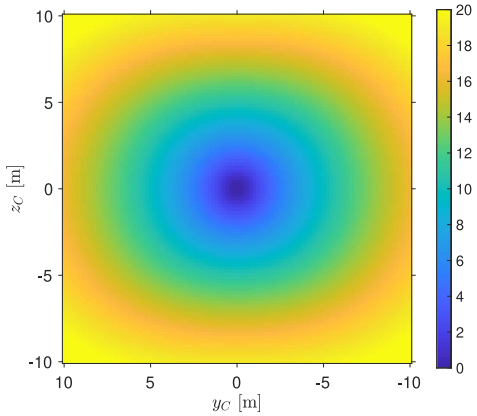

(a) $\mathrm{RCRB_u}(x_C)$ as a function of y_C and z_C

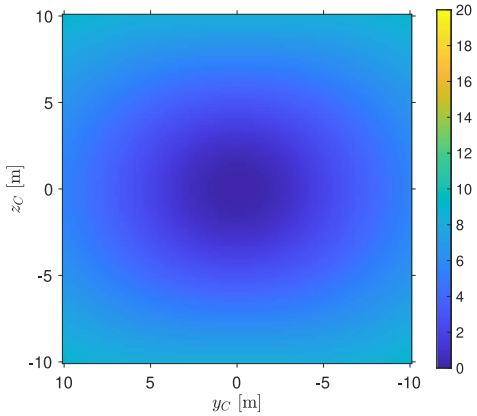

(b) $\mathrm{RCRB_u}(y_C)$ as a function of y_C and z_C

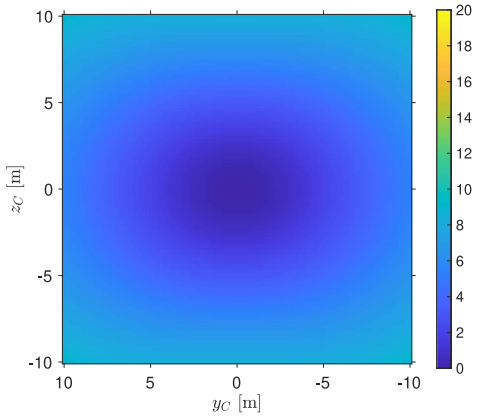

(c) $\mathrm{RCRB_u}(z_C)$ as a function of y_C and z_C

Fig. 6. RCRBs in the case of unknown orientation as a function of y_C and z_C when $x_C = 6$ m. The dipole is oriented vertically and $L = 3$ m.

the blue zones in each figure correspond to the best estimation accuracy. Fig. 6 clearly shows the different behaviours of various RCRBs when the dipole moves away from the CPL position. For example, we see that $\mathrm{RCRB_u}(x_C)$ increases faster than $\mathrm{RCRB_u}(y_C)$ and $\mathrm{RCRB_u}(z_C)$ whatever the direction of motion is. On the other hand, $\mathrm{RCRB_u}(y_C)$ and $\mathrm{RCRB_u}(z_C)$ have a similar behavior. The same conclusions hold when the dipole orientation is known.

From the above analyses, we conclude that the CRBs are approximately the same whether or not the orientation of the

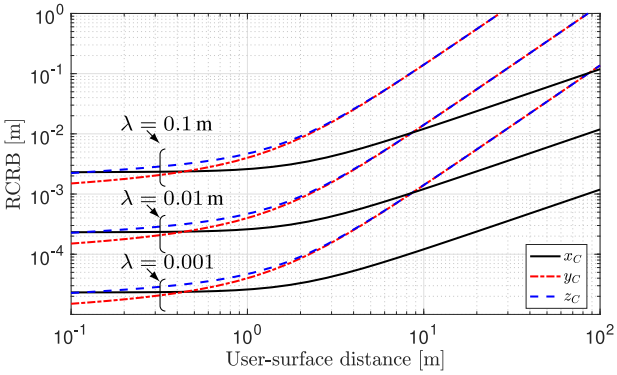

Fig. 7. RCRBs as a function of x_C for a vertical dipole in CPL and $L = 3$ m, with $\lambda = 0.1,\ 0.01$ or 0.001 m.

transmitting dipole is known. However, this does not necessarily mean that we can ignore the effect of dipole orientation in the estimation process. It only means that the joint estimation of $\hat{\mathbf{t}}$ and $\mathbf{u}$ ultimately provides the same localization accuracy as if $\hat{\mathbf{t}}$ were known. The impact of the orientation knowledge will be quantified in Section VI where MLEs will be considered.

C. Impact of Carrier Frequency

Fig. 7 shows the RCRBs as a function of x_C for three different values of the wavelength, namely $\lambda = 0.1$ m (corresponding to $f_c = 3$ GHz), $\lambda = 0.01$ m (corresponding to $f_c = 30$ GHz) and $\lambda = 0.001$ m (corresponding to $f_c = 300$ GHz). The dipole is in CPL and is oriented vertically. Its orientation is unknown to the receiver. The surface side length is $L = 3$ m. As expected, the estimation accuracy reduces as the distance between the source and the observation region increases. In particular, we see that $\mathrm{RCRB}(x_C)$ increases *slower* than $\mathrm{RCRB}(y_C)$ and $\mathrm{RCRB}(z_C)$. Notice that the RCBRs depend linearly on λ, at least in the range of values of x_C (and hence ρ) considered in Fig. 7. Indeed, reducing the wavelength by a factor of 10 reduces the RCBRs of the same factor. This can easily be derived analytically for x_C and y_C by considering the results in Proposition 2. This holds true also for z_C, as it is shown in Fig. 7. Notice that the same dependence on λ was already observed in [8]. Similar results (not shown due to space limitations) can be obtained if the dipole orientation is known. Marginal differences are only observed for $\lambda = 0.1$ m and small values of L, i.e., $L \leq 0.1$ m.

VI. Evaluating the Impact of Different Models

To show how different electric field models impact the estimation accuracy, we now use the derived CRBs to benchmark different MLEs derived on the basis of a discrete representation of misspecified models. Particularly, we consider a practical scenario in which the observation region is filled with vertically-oriented short dipoles. The analysis is carried out under the hypotheses of Assumption 1 for $l_s = \lambda/4$ and $\lambda = 0.1$. Since $2l_s^2/\lambda = \lambda/8 = 0.0125$ m, this means that it is valid for all distances of practical relevance.

Remark 2: *When the assumed model differs from the true one, the estimation problem is said to be misspecified or mismatched [33], [34]. In these circumstances, fundamental limits can be computed by resorting to the mismatched estimation theory, which allows to derive the CRBs under model mismatching. This is without any doubt an interesting extension of our theoretical analysis, which is left for future work. A comprehensive review on the subject can be found in [35].*

A. Discrete Signal Model

We assume that the observation region is filled with short dipoles of length $l_r = \lambda/10$, vertically oriented and placed on a square grid. The centers of the dipoles are the set of points of $\mathcal{R}_o$ given by $\{(x, y, z) : x = 0, y = m\lambda/2, z = n\lambda/2\}$, with $1 \leq |m|, |n| \leq N_r$ and $N_r = \lfloor L/\lambda \rfloor$. The voltage V_{mn} observed at the output of the (m, n) receive dipole is obtained by integrating over the antenna length the vertical component given by

$$\xi_z(\mathbf{r}) = e_z(\mathbf{r}) + n_z(\mathbf{r}). \tag{82}$$

Since the Hertzian dipole is electrically small, i.e., $l_r \ll \lambda$, it follows that V_{mn} can be approximated as

$$V_{mn} = \int_{l_r} \xi_z(\mathbf{r}) dz \approx h_{mn} + \nu_{mn} \tag{83}$$

where

$$h_{mn} = l_r e_z(\mathbf{r}_{mn}) \tag{84}$$

with $\mathbf{r}_{mn} = x_C\hat{\mathbf{x}} + (y_m - y_C)\hat{\mathbf{y}} + (z_n - z_C)\hat{\mathbf{z}}$, and $\{\nu_{mn}\}$ are independent zero-mean gaussian random variables, with variance $\sigma_\nu^2 = 2\sigma^2 l_r/\lambda$.

B. Maximum-Likelihood Estimation Under Misspecified Models

The log-likelihood function for the estimation of $\hat{\mathbf{t}} = (t_x, t_y, t_z)$ and $\mathbf{u} = (x_C, y_C, z_C)$ on the basis of the observations $\{V_{mn}; |m|, |n| = 1, \ldots, N_r\}$ is given by [31, Ch. 7]

$$\Lambda(\tilde{\mathbf{t}}, \tilde{\mathbf{u}}) = -\sum_{|m|,|n|=1,\ldots,N_r} \sum |V_{mn} - \tilde{h}_{mn}|^2 \tag{85}$$

where $\tilde{\mathbf{t}} = (\tilde{t}_x, \tilde{t}_y, \tilde{t}_z)$ and $\tilde{\mathbf{u}} = (\tilde{x}_C, \tilde{y}_C, \tilde{z}_C)$ are trial values for $\hat{\mathbf{t}}$ and $\mathbf{u}$, respectively, and $\tilde{h}_{mn}$ is obtained accordingly. Different MLEs can be obtained if different models are assumed for $\tilde{h}_{mn}$ in (85). Specifically, we consider the following three.

1) The first MLE (MLE1) relies on the model provided in (42) and assumes that:
$$h_{mn}^{(1)} = l_r e_z(\mathbf{r}_{mn}). \tag{86}$$
2) The second MLE (MLE2) makes use of the signal model adopted in [8]. Hence, we have that:
$$h_{mn}^{(2)} = l_r G(r)\sqrt{\frac{x_C}{r}}. \tag{87}$$
3) The third MLE (MLE3) is based on the standard planar approximation (38) under which:
$$h_{mn}^{(3)} = l_r G(r_C) e^{-\mathrm{j}k(\hat{\mathbf{r}}_C \cdot \mathbf{d}_{mn})} \tag{88}$$
with $\mathbf{d}_{mn} = y_m\hat{\mathbf{y}} + z_n\hat{\mathbf{z}}$. Notice that with the standard planar wave model, the amplitude of the received signal is proportional to $1/r_C$. Such a dependence can effectively be exploited for the estimation of r_C provided that the proportionality factor is exactly known.

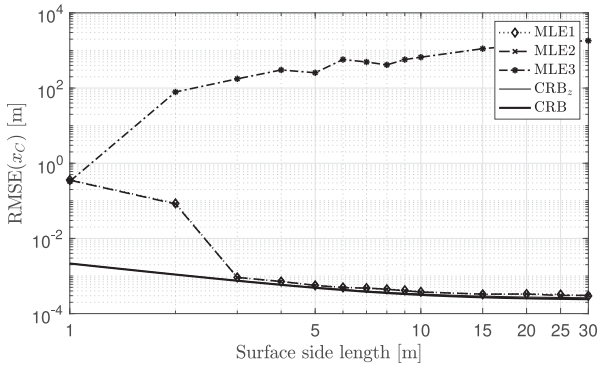

(a) Estimation accuracy for x_C

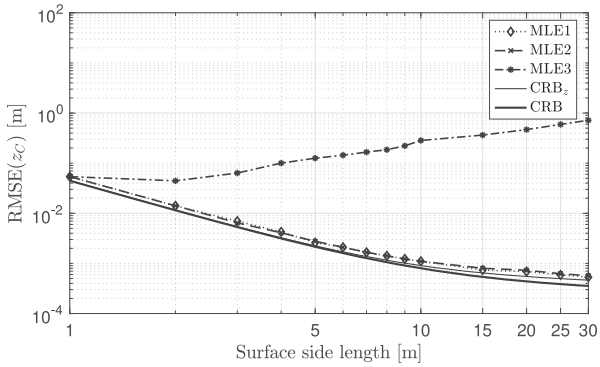

(b) Estimation accuracy for z_C

Fig. 8. Comparisons between MLEs when $\hat{\mathbf{t}} = (0, 0, 1)$.

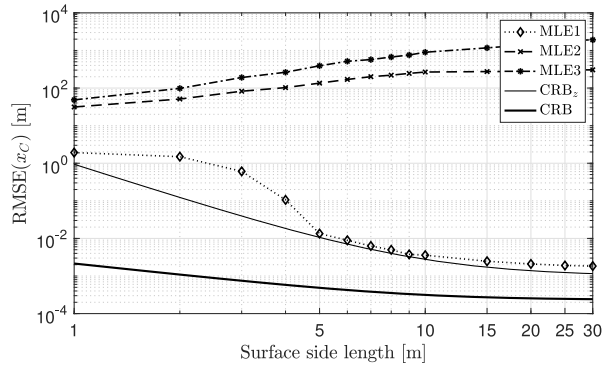

(a) Estimation accuracy for x_C

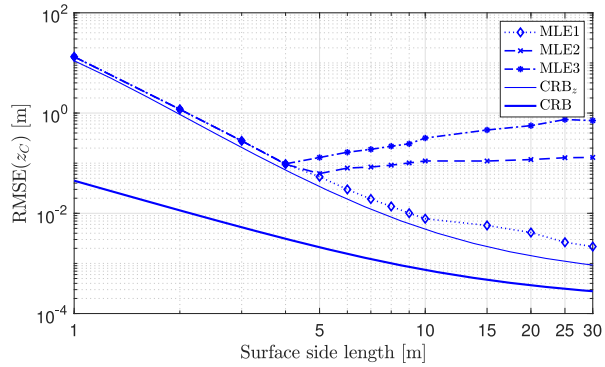

(b) Estimation accuracy for z_C

Fig. 9. Comparisons between MLEs when $\hat{\mathbf{t}} = (0, 1, 0)$.

The first MLE takes the form

$$\hat{\mathbf{t}}^{(1)}, \mathbf{u}^{(1)} = \arg\max_{\tilde{\mathbf{t}}, \tilde{\mathbf{u}}} \Lambda^{(1)}(\tilde{\mathbf{t}}, \tilde{\mathbf{u}}) \tag{89}$$

where

$$\Lambda^{(1)}(\tilde{\mathbf{t}}, \tilde{\mathbf{u}}) = -\sum_{|m|,|n|=1,\ldots,N_r} \sum |V_{mn} - \tilde{h}_{mn}^{(1)}|^2. \tag{90}$$

In case of known orientation, the maximization of (89) is carried out only over $\tilde{\mathbf{u}}$, after replacing $\tilde{\mathbf{t}}$ with the true value $\hat{\mathbf{t}}$ in $\tilde{h}_{mn}^{(1)}$.

The MLEs derived from (87)–(88) are in the following form:

$$\mathbf{u}^{(i)} = \arg\max_{\tilde{\mathbf{u}}} \Lambda^{(i)}(\tilde{\mathbf{u}}) \tag{91}$$

where

$$\Lambda^{(i)}(\tilde{\mathbf{u}}) = -\sum_{|m|,|n|=1,\ldots,N_r} \sum |V_{mn} - \tilde{h}_{mn}^{(i)}|^2 \tag{92}$$

for $i = 2, 3$. Notice that (91) needs to be optimized only with respect to $\tilde{\mathbf{u}}$. This is because $h_{mn}^{(2)}$ and $h_{mn}^{(3)}$ do not account for the dependence of the received signal on the orientation of the source dipole. This will have a profound impact on the estimators' performance.

C. Numerical Analysis

The accuracy of the above three MLEs is now quantified in terms of the square root of the MSE (RMSE), measured in meters and given by

$$\mathrm{RMSE}(\upsilon) = \sqrt{\mathrm{E}(\upsilon - \hat{\upsilon})^2} \tag{93}$$

where υ stands for x_C, y_C or z_C, and $\hat{\upsilon}$ is the corresponding ML estimate. The estimation accuracy of the three MLEs is compared with the provided CRBs. Since V_{mn} is obtained by integrating ξ_z, we also report CRB_z, which is derived from the observation of the only z-component of the electric field.

Fig. 8(a) shows $\mathrm{RMSE}(x_C)$ as a function of L, measured in meters. The transmitting dipole is in CPL, with $x_C = 6$ m, and is vertically oriented, i.e., $\hat{\mathbf{t}} = (0, 0, 1)$. The wavelength is $\lambda = 0.1$ m, and $\mathrm{SNR} = 30$ dB. The following interesting conclusions can be drawn from the results in Fig. 8(a):

- A negligible difference is observed between $\mathrm{CRB}(x_C)$ and $\mathrm{CRB}_z(x_C)$. This means that, when the transmit and receive dipoles have the same orientation, the component of the electric field along the dipoles' orientation provides almost all the information about the source position.
- MLE1 performs closely to the CRB in both cases of known and unknown orientation. This confirms the results from Section V, in which it has been shown that CRB and CRB_u are practically the same.
- When the transmit dipole is vertically oriented, the estimation accuracy achieved with MLE2 is the same as that with MLE1.
- MLE3 has poor performance and its estimation accuracy worsens as L grows. This is due to the fact that the underlying planar model in (88) becomes more and more inaccurate as the surface side length gets larger.

The same observations are valid for y_C and z_C. For example, Fig. 8(b) shows $\mathrm{RMSE}(z_C)$ in the same setting of Fig. 8(a). We see that MLE1 and MLE2 have similar behaviors, and are very

close to $\mathrm{CRB}_z(z_C)$, while MLE3 is far from the bound. A slight difference is observed between $\mathrm{CRB}(z_C)$ and $\mathrm{CRB}_z(z_C)$, for $L > 5$ m.

Fig. 9(a) illustrates $\mathrm{RMSE}(x_C)$ assuming that the transmitting dipole is oriented along the y-direction, i.e., $\hat{\mathbf{t}} = (0, 1, 0)$. The other parameters are the same as in Fig. 8(a). Compared to Fig. 8(a), we observe two fundamental differences. First, $\mathrm{CRB}(x_C)$ and $\mathrm{CRB}_z(x_C)$ differ significantly. This means that, in general, to achieve the best estimation accuracy all the components of the electric field should be considered. Secondly, MLE2 has poor performance, because it ignores the dependence of the received signal on the orientation of the transmit dipole. This confirms the importance of the term $[\hat{\mathbf{r}}\times\mathbf{R}(\theta,\phi)]\times\hat{\mathbf{r}}$ in (7), which is not considered in the standard models adopted in literature. Thirdly, the estimation accuracy with both MLE2 and MLE3 get worse as the surface side length gets larger due to the increasing inaccuracy of the underlying wave models in (87) and (88), respectively. Similar conclusions can be drawn from the plots in Fig. 9(b), which show the accuracy in the estimation of z_C. In this case, we see that the performance of MLE1 differs from $\mathrm{CRB}_z(x_C)$ only for $L > 10$ m, where the estimation accuracy is anyway better than 1 cm.

VII. Conclusion

Large antenna arrays and high frequencies opens up opportunities for new signal processing algorithms for positioning. Motivated by the need of establishing ultimate bounds, we provided a general model for the electric vector field over a spatially-continuous rectangular region. Unlike standard models in signal processing, the functional dependence on the radiation vector at the source is intrinsically captured by the model. The electric vector field model was used to compute the CRBs for the three-dimensional (3D) spatial location of a Hertzian dipole, with and without a priori knowledge of its orientation. Further simplifications and insights were obtained by assuming that the dipole center is located on the line perpendicular to the surface center. Numerical results showed that a centimeter-level accuracy in the mmWave and sub-THz bands can only be achieved with surfaces of size in the range of a few meters. Asymptotic expressions were also given in closed-form to show the scaling behaviors with respect to surface area and wavelength. To show how different electric field models impact the estimation accuracy, we used the derived CRBs to benchmark different MLEs. The analysis showed that the standard model neglecting the radiation angular pattern of the transmitting source may provide low estimation accuracy in the presence of large surfaces.

The statements above do not want to mean that the standard model is not useful. Only that its limitations need to be clearly acknowledged and understood, and its performance carefully evaluated on a case-by-case basis. The standard models may be sufficiently accurate in some situations and inadequate in others. It is essential to evaluate the performance of algorithms based on the standard model against data generated using the analytic model.

Appendix A

We compute the derivatives of the cartesian components of the electric field with respect to the unknown parameters $(t_x, t_y, t_z, x_C, y_C, z_C)$. Starting from (43)–(45), after lengthy but standard calculations we have

$$\frac{\partial e_\alpha}{\partial t_\beta} = -\,\mathrm{j}\,\chi\frac{\mathrm{e}^{-\mathrm{j}\,kr}}{r}\cdot\begin{cases}1-r_\alpha^2 & \text{per}\quad \beta=\alpha,\\ -r_\alpha r_\beta & \text{per}\quad \beta\neq\alpha\end{cases} \tag{94}$$

with $\alpha, \beta \in \{x, y, z\}$ and r_α being defined in (47),

$$\frac{\partial e_x}{\partial x_C} = \frac{-\,\mathrm{j}\,\chi\mathrm{e}^{-\mathrm{j}\,kr}}{r^4}\left\{\mathrm{j}\,k\bar{x}\left[t_x(\bar{y}^2+\bar{z}^2)-\bar{x}(t_y\bar{y}+t_z\bar{z})\right] + \frac{3t_x\bar{x}(\bar{y}^2+\bar{z}^2)-(t_y\bar{y}+t_z\bar{z})(2\bar{x}^2-\bar{y}^2-\bar{z}^2)}{r}\right\} \tag{95a}$$

$$\frac{\partial e_x}{\partial y_C} = \frac{-\,\mathrm{j}\,\chi\mathrm{e}^{-\mathrm{j}\,kr}}{r^4}\left\{\mathrm{j}\,k\bar{y}\left[t_x(\bar{y}^2+\bar{z}^2)-\bar{x}(t_y\bar{y}+t_z\bar{z})\right] - \frac{t_x\bar{y}(2\bar{x}^2-\bar{y}^2-\bar{z}^2)-t_y\bar{x}(\bar{x}^2-2\bar{y}^2+\bar{z}^2)+3t_z\bar{x}\bar{y}\bar{z}}{r}\right\} \tag{95b}$$

$$\frac{\partial e_x}{\partial z_C} = \frac{-\,\mathrm{j}\,\chi\mathrm{e}^{-\mathrm{j}\,kr}}{r^4}\left\{\mathrm{j}\,k\bar{z}\left[t_x(\bar{y}^2+\bar{z}^2)-\bar{x}(t_y\bar{y}+t_z\bar{z})\right] - \frac{t_x\bar{z}(2\bar{x}^2-\bar{y}^2-\bar{z}^2)+3t_y\bar{x}\bar{y}\bar{z}-t_z\bar{x}(\bar{x}^2+\bar{y}^2-2\bar{z}^2)}{r}\right\} \tag{95c}$$

$$\frac{\partial e_y}{\partial x_C} = \frac{-\,\mathrm{j}\,\chi\mathrm{e}^{-\mathrm{j}\,kr}}{r^4}\left\{\mathrm{j}\,k\bar{x}\left[t_y(\bar{x}^2+\bar{z}^2)-\bar{y}(t_x\bar{x}+t_z\bar{z})\right] - \frac{t_y\bar{x}(2\bar{y}^2-\bar{x}^2-\bar{z}^2)-t_x\bar{y}(\bar{y}^2-2\bar{x}^2+\bar{z}^2)+3t_z\bar{x}\bar{y}\bar{z}}{r}\right\} \tag{96a}$$

$$\frac{\partial e_y}{\partial y_C} = \frac{-\,\mathrm{j}\,\chi\mathrm{e}^{-\mathrm{j}\,kr}}{r^4}\left\{\mathrm{j}\,k\bar{y}\left[t_y(\bar{x}^2+\bar{z}^2)-\bar{y}(t_x\bar{x}+t_z\bar{z})\right] + \frac{3t_y\bar{y}(\bar{x}^2+\bar{z}^2)-(t_x\bar{x}+t_z\bar{z})(2\bar{y}^2-\bar{x}^2-\bar{z}^2)}{r}\right\} \tag{96b}$$

$$\frac{\partial e_y}{\partial z_C} = \frac{-\,\mathrm{j}\,\chi\mathrm{e}^{-\mathrm{j}\,kr}}{r^4}\left\{\mathrm{j}\,k\bar{z}\left[t_y(\bar{x}^2+\bar{z}^2)-\bar{y}(t_x\bar{x}+t_z\bar{z})\right] - \frac{t_y\bar{z}(2\bar{y}^2-\bar{x}^2-\bar{z}^2)+3t_x\bar{x}\bar{y}\bar{z}-t_z\bar{y}(\bar{x}^2+\bar{y}^2-2\bar{z}^2)}{r}\right\} \tag{96c}$$

$$\frac{\partial e_z}{\partial x_C} = \frac{-\,\mathrm{j}\,\chi\mathrm{e}^{-\mathrm{j}\,kr}}{r^4}\left\{\mathrm{j}\,k\bar{x}\left[t_z(\bar{x}^2+\bar{y}^2)-\bar{z}(t_x\bar{x}+t_y\bar{y})\right] - \frac{t_z\bar{x}(2\bar{z}^2-\bar{x}^2-\bar{y}^2)+3t_y\bar{x}\bar{y}\bar{z}-t_x\bar{z}(\bar{z}^2+\bar{y}^2-2\bar{x}^2)}{r}\right\} \tag{97a}$$

$$\frac{\partial e_z}{\partial y_C} = \frac{-\,\mathrm{j}\,\chi\mathrm{e}^{-\mathrm{j}\,kr}}{r^4}\left\{\mathrm{j}\,k\bar{y}\left[t_z(\bar{x}^2+\bar{y}^2)-\bar{z}(t_x\bar{x}+t_y\bar{y})\right] - \frac{t_z\bar{y}(2\bar{z}^2-\bar{x}^2-\bar{y}^2)-t_y\bar{z}(\bar{z}^2-2\bar{y}^2+\bar{x}^2)+3t_x\bar{x}\bar{y}\bar{z}}{r}\right\} \tag{97b}$$

$$\frac{\partial e_z}{\partial z_C} = \frac{-\mathrm{j}\,\chi \mathrm{e}^{-\mathrm{j}\,kr}}{r^4}\left\{\mathrm{j}\,k\bar{z}\left[t_z(\bar{x}^2+\bar{y}^2)-\bar{z}(t_x\bar{x}+t_y\bar{y})\right] + \frac{3t_z\bar{z}(\bar{x}^2+\bar{y}^2)-(t_x\bar{x}+t_y\bar{y})(2\bar{z}^2-\bar{y}^2-\bar{x}^2)}{r}\right\}. \tag{97c}$$

For convenience, we have set $\bar{x} = -x_C$, $\bar{y} = y - y_C$ e $\bar{z} = z - z_C$.

Appendix B

In this appendix, we prove the results of Proposition 1. We start by observing that, under Assumption 5, the derivatives needed for the computation of FIM in (49) are obtained from the equations in Appendix A by simply setting $y_C = z_C = 0$, $t_x = t_y = 0$ and $t_z = 1$.

We first computate the elements of $\mathbf{F}_{cc}$ given by

$$[\mathbf{F}_{cc}]_{mn} = \frac{2}{\sigma^2}\mathrm{Re}\left\{\int_{-\frac{L}{2}}^{\frac{L}{2}}\int_{-\frac{L}{2}}^{\frac{L}{2}} f_{mn}^{(cc)}(y,z)dydz\right\} \tag{98}$$

where

$$f_{mn}^{(cc)}(y,z) = \frac{\partial e_x(\mathbf{r})}{\partial a_m}\frac{\partial e_x^*(\mathbf{r})}{\partial a_n} + \frac{\partial e_y(\mathbf{r})}{\partial a_m}\frac{\partial e_y^*(\mathbf{r})}{\partial a_n} + \frac{\partial e_z(\mathbf{r})}{\partial a_m}\frac{\partial e_z^*(\mathbf{r})}{\partial a_n} \tag{99}$$

with $a_1 = x_C$, $a_2 = y_C$ and $a_3 = z_C$. In this case, it can be shown that, for $m \neq n$, $f_{mn}^{(cc)}(y,z)$ in (99) is an odd function of y and z, i.e.,

$$f_{mn}^{(cc)}(y,z) = -f_{mn}^{(cc)}(-y,z) = -f_{mn}^{(cc)}(y,-z).$$

As a result, due to the symmetry of the integration domain, the off-diagonal elements of $\mathbf{F}_{cc}$ are zero, meaning that $\mathbf{F}_{cc}$ is a diagonal matrix. As for the diagonal elements, standard but lengthy calculations show that they can be written as in (63)–(65) where

$$\mathcal{I}_1 \triangleq \frac{\rho}{(4+\rho^2)}\left[\frac{(14+3\rho^2)}{\sqrt{4+\rho^2}}\arctan\frac{\rho}{\sqrt{4+\rho^2}} + \frac{\rho}{(2+\rho^2)}\right] \tag{100}$$

$$\mathcal{I}_2 \triangleq \int_{-\rho/2}^{\rho/2}\int_{-\rho/2}^{\rho/2}\frac{1+u^2v^2+v^4}{(1+u^2+v^2)^4}dudv \tag{101}$$

$$\mathcal{I}_3 \triangleq \int_{-\rho/2}^{\rho/2}\int_{-\rho/2}^{\rho/2}\frac{u^2(1+u^2)}{(1+u^2+v^2)^3}dudv \tag{102}$$

$$\mathcal{I}_4 \triangleq \int_{-\rho/2}^{\rho/2}\int_{-\rho/2}^{\rho/2}\frac{u^2(1+u^2)+v^2(1+v^2)-u^2v^2}{(1+u^2+v^2)^4}dudv \tag{103}$$

$$\mathcal{I}_5 \triangleq \int_{-\rho/2}^{\rho/2}\int_{-\rho/2}^{\rho/2}\frac{v^2(1+u^2)}{(1+u^2+v^2)^3}dudv \tag{104}$$

$$\mathcal{I}_6 \triangleq \frac{\rho}{2(4+\rho^2)^2}\left[\frac{(9\rho^4+76\rho^2+136)}{\sqrt{4+\rho^2}}\arctan\frac{\rho}{\sqrt{4+\rho^2}} + \frac{\rho(3\rho^4+4\rho^2-8)}{(2+\rho^2)^2}\right] \tag{105}$$

with $\rho = L/x_C$. Now, we consider the computation of $\mathbf{F}_{tt}$ with elements

$$[\mathbf{F}_{tt}]_{mn} = \frac{2}{\sigma^2}\mathrm{Re}\left\{\int_{-\frac{L}{2}}^{\frac{L}{2}}\int_{-\frac{L}{2}}^{\frac{L}{2}} f_{mn}^{(tt)}(y,z)dydz\right\} \tag{106}$$

where

$$f_{mn}^{(tt)}(y,z) = \frac{\partial e_x(\mathbf{r})}{\partial b_m}\frac{\partial e_x^*(\mathbf{r})}{\partial b_n} + \frac{\partial e_y(\mathbf{r})}{\partial b_m}\frac{\partial e_y^*(\mathbf{r})}{\partial b_n} + \frac{\partial e_z(\mathbf{r})}{\partial b_m}\frac{\partial e_z^*(\mathbf{r})}{\partial b_n} \tag{107}$$

with $b_1 = t_x$, $b_2 = t_y$ and $b_3 = t_z$. Again, it can easily be shown that, for $m \neq n$, $f_{mn}^{(tt)}(y,z)$ in (107) is an odd function of y or z, and hence the off-diagonal elements of $\mathbf{F}_{tt}$ are zero, meaning that $\mathbf{F}_{tt}$ is diagonal. The diagonal elements can be written as in (66)–(67) where

$$\mathcal{I}_7 \triangleq \int_{-\rho/2}^{\rho/2}\int_{-\rho/2}^{\rho/2}\frac{u^2+v^2}{(1+u^2+v^2)^2}dudv \tag{108}$$

$$\mathcal{I}_8 \triangleq \int_{-\rho/2}^{\rho/2}\int_{-\rho/2}^{\rho/2}\frac{1+u^2}{(1+u^2+v^2)^2}dudv. \tag{109}$$

Consider now the matrix $\mathbf{F}_{tc}$ with elements given by

$$[\mathbf{F}_{tc}]_{mn} = \frac{2}{\sigma^2}\mathrm{Re}\left\{\int_{-\frac{L}{2}}^{\frac{L}{2}}\int_{-\frac{L}{2}}^{\frac{L}{2}} f_{mn}^{(tc)}(y,z)dydz\right\} \tag{110}$$

where

$$f_{mn}^{(tc)}(y,z) = \frac{\partial e_x(\mathbf{r})}{\partial b_m}\frac{\partial e_x^*(\mathbf{r})}{\partial a_n} + \frac{\partial e_y(\mathbf{r})}{\partial b_m}\frac{\partial e_y^*(\mathbf{r})}{\partial a_n} + \frac{\partial e_z(\mathbf{r})}{\partial b_m}\frac{\partial e_z^*(\mathbf{r})}{\partial a_n} \tag{111}$$

and a_n, b_m have the same meaning as before. It can be shown that $f_{13}^{(tc)}(y,z)$ and $f_{31}^{(tc)}(y,z)$ are even functions of y and z whereas the others are odd functions of y or z. As a consequence, the only non-zero entries of $\mathbf{F}_{tc}$ are $[\mathbf{F}_{tc}]_{13}$ and $[\mathbf{F}_{tc}]_{31}$ given by (68) and (69), respectively, where

$$\mathcal{I}_9 \triangleq \frac{2\rho}{4+\rho^2}\left[\frac{2+\rho^2}{\sqrt{4+\rho^2}}\arctan\frac{\rho}{\sqrt{4+\rho^2}} - \frac{\rho}{2+\rho^2}\right] \tag{112}$$

$$\mathcal{I}_{10} \triangleq \int_{-\rho/2}^{\rho/2}\int_{-\rho/2}^{\rho/2}\frac{(1+2\,u^2)}{(1+u^2+v^2)^4}dudv. \tag{113}$$

Appendix C

The proof of Proposition 2 is given. We start by deriving (76). As a first step, we show that $k^2\mathcal{I}_1 \gg x_C^{-2}\mathcal{I}_2$, for $x_C \gg \lambda$. To this end, observe that

$$\mathcal{I}_1 = \int_{-\rho/2}^{\rho/2}\int_{-\rho/2}^{\rho/2}\frac{1+v^2}{(1+u^2+v^2)^3}dudv. \tag{114}$$

Comparing (114) and (101) yields $\mathcal{I}_1 > \mathcal{I}_2$ since

$$\frac{1+v^2}{(1+u^2+v^2)^3} \geq \frac{1+u^2v^2+v^4}{(1+u^2+v^2)^4}. \tag{115}$$

Since $0 \leq \mathcal{I}_2 - \mathcal{I}_8^{-1}\mathcal{I}_{10}^2 < \mathcal{I}_2$ (notice that $\mathcal{I}_2 - \mathcal{I}_8^{-1}\mathcal{I}_{10}^2$ must necessarily be non-negative and $\mathcal{I}_8^{-1}\mathcal{I}_{10}^2 > 0$), for $x_C \gg \lambda$ we have

$$4\pi^2\lambda^{-2}\mathcal{I}_1 \gg x_C^{-2}\mathcal{I}_2 > x_C^{-2}\left(\mathcal{I}_2 - \mathcal{I}_8^{-1}\mathcal{I}_{10}^2\right). \tag{116}$$

The approximation in (76) derives from (116) immediately.

We now derive (77) by showing that $k^2\mathcal{I}_3 \gg x_C^{-2}\mathcal{I}_4$. Observe that

$$0 < \mathcal{I}_4 < \int_{-\rho/2}^{\rho/2}\int_{-\rho/2}^{\rho/2} \frac{2\,u^2(1+u^2)}{(1+u^2+v^2)^4} du dv < 2\,\mathcal{I}_3 \quad (117)$$

from which we easily obtain

$$4\pi^2\lambda^{-2}\mathcal{I}_3 \gg x_C^{-2}\mathcal{I}_4 \quad (118)$$

for $x_C \gg \lambda$. The approximation in (77) follows from (118) immediately.

Appendix D

The analysis of the CRBs in the asymptotic regime $\rho \to \infty$ requires the computation of the following limits:

1) $\lim_{\rho\to\infty} \mathcal{I}_1$
2) $\lim_{\rho\to\infty} \mathcal{I}_3$
3) $\lim_{\rho\to\infty} (k^2\mathcal{I}_5 + x_C^{-2}\mathcal{I}_6)$
4) $\lim_{\rho\to\infty} [k^2\mathcal{I}_5 + x_C^{-2}(\mathcal{I}_6 - \mathcal{I}_7^{-1}\mathcal{I}_9^2)]$.

We start by evaluating the first. From (100), we have

$$\lim_{\rho\to\infty} \mathcal{I}_1 = 3\pi/4. \quad (119)$$

Consider now $\mathcal{I}_3$. Due to the non-negativity of the function $u^2(1+u^2)/(1+u^2+v^2)^3$, we have

$$\int_{\mathcal{C}^-} \frac{u^2(1+u^2)}{(1+u^2+v^2)^3} du dv < \mathcal{I}_3 < \int_{\mathcal{C}^+} \frac{u^2(1+u^2)}{(1+u^2+v^2)^3} du dv \quad (120)$$

The two integrals can be computed in closed form. In particular, we obtain

$$\int_{\mathcal{C}^-} \frac{u^2(1+u^2)}{(1+u^2+v^2)^3} du dv = \frac{3\pi}{8}\ln(1+\rho^2) - \frac{\pi}{16}\frac{\rho^2(5\rho^2+6)}{(1+\rho^2)^2} \quad (121)$$

$$\int_{\mathcal{C}^+} \frac{u^2(1+u^2)}{(1+u^2+v^2)^3} du dv = \frac{3\pi}{8}\ln(1+2\rho^2) - \frac{\pi}{4}\frac{\rho^2(5\rho^2+3)}{(1+2\rho^2)^2}. \quad (122)$$

Taking (120) and (121)–(122) into account yields

$$\mathcal{I}_3 \sim \frac{3\pi}{4}\ln\rho \qquad \text{as } \rho \to \infty \quad (123)$$

from which (79) is derived straightforwardly.

Now, we focus on the limits

$$\lim_{\rho\to\infty} \left(k^2\mathcal{I}_5 + x_C^{-2}\mathcal{I}_6\right) \quad (124)$$

and

$$\lim_{\rho\to\infty} \left[k^2\mathcal{I}_5 + x_C^{-2}\left(\mathcal{I}_6 - \mathcal{I}_7^{-1}\mathcal{I}_9^2\right)\right]. \quad (125)$$

By using similar arguments to those for $\mathcal{I}_3$, it can be shown that

$$\mathcal{I}_5 \sim \frac{\pi}{4}\ln\rho \qquad \text{as } \rho \to \infty. \quad (126)$$

and

$$\lim_{\rho\to\infty} \mathcal{I}_7 = \infty. \quad (127)$$

As for $\mathcal{I}_6$ and $\mathcal{I}_9$, from (105) and (112) we have that

$$\lim_{\rho\to\infty} \mathcal{I}_6 = 9\pi/8. \quad (128)$$

and

$$\lim_{\rho\to\infty} \mathcal{I}_9 = \pi/2. \quad (129)$$

By taking (126)–(129) into account, (80) follows easily.

References

[1] A. D. J. Torres, A. A. D'Amico, L. Sanguinetti, and M. Z. Win, "Cramér-Rao bounds for near-field localization," in *Proc. Asilomar Conf. Signals, Syst., Comput.*, 2021, pp. 1250–1254. [Online]. Available: https://arxiv.org/abs/2104.14825

[2] 3GPP, "Technical specification group services and system aspects (release 16)," 3GPP Tech. Rep. TR 21.916 V16.1.0, Jan. 2022.

[3] J. Lee et al., "Spectrum for 5G: Global status, challenges, and enabling technologies," *IEEE Commun. Mag.*, vol. 56, no. 3, pp. 12–18, Mar. 2018.

[4] D. Dardari and N. Decarli, "Holographic communication using intelligent surfaces," *IEEE Commun. Mag.*, vol. 59, no. 6, pp. 35–41, Jun. 2021.

[5] C. Huang et al., "Holographic MIMO surfaces for 6G wireless networks: Opportunities, challenges, and trends," *IEEE Wireless Commun.*, vol. 27, no. 5, pp. 118–125, Oct. 2020.

[6] A. Pizzo, T. L. Marzetta, and L. Sanguinetti, "Spatially-stationary model for holographic MIMO small-scale fading," *IEEE J. Sel. Areas Commun.*, vol. 38, no. 9, pp. 1964–1979, Sep. 2020.

[7] S. Hu, F. Rusek, and O. Edfors, "Beyond massive MIMO: The potential of data transmission with large intelligent surfaces," *IEEE Trans. Signal Process.*, vol. 66, no. 10, pp. 2746–2758, May 2018.

[8] S. Hu, F. Rusek, and O. Edfors, "Beyond massive MIMO: The potential of positioning with large intelligent surfaces," *IEEE Trans. Signal Process.*, vol. 66, no. 7, pp. 1761–1774, Apr. 2018.

[9] E. Basar, M. Di Renzo, J. De Rosny, M. Debbah, M. Alouini, and R. Zhang, "Wireless communications through reconfigurable intelligent surfaces," *IEEE Access*, vol. 7, pp. 116753–116773, 2019.

[10] M. Di Renzo et al., "Smart radio environments empowered by reconfigurable intelligent surfaces: How it works, state of research, and the road ahead," *IEEE J. Sel. Areas Commun.*, vol. 38, no. 11, pp. 2450–2525, Nov. 2020.

[11] A. Bourdoux et al., "6G white paper on localization and sensing," 2020. [Online]. Available: https://arxiv.org/abs/2006.01779

[12] B. Friedlander, "Localization of signals in the near-field of an antenna array," *IEEE Trans. Signal Process.*, vol. 67, no. 15, pp. 3885–3893, Aug. 2019.

[13] J.-S. Jiang and M. Ingram, "Spherical-wave model for short-range MIMO," *IEEE Trans. Commun.*, vol. 53, no. 9, pp. 1534–1541, Sep. 2005.

[14] F. Bohagen, P. Orten, and G. E. Oien, "On spherical vs. plane wave modeling of line-of-sight MIMO channels," *IEEE Trans. Commun.*, vol. 57, no. 3, pp. 841–849, Mar. 2009.

[15] J. Yang, Y. Zeng, S. Jin, C.-K. Wen, and P. Xu, "Communication and localization with extremely large lens antenna array," *IEEE Trans. Wireless Commun.*, vol. 20, no. 5, pp. 3031–3048, May 2021.

[16] J. V. Alegria and F. Rusek, "Cramér-rao lower bounds for positioning with large intelligent surfaces using quantized amplitude and phase," in *Proc. 53rd Asilomar Conf. Signals, Syst., Comput.*, 2019, pp. 10–14.

[17] F. Guidi and D. Dardari, "Radio positioning with EM processing of the spherical wavefront," *IEEE Trans. Wireless Commun.*, vol. 20, no. 6, pp. 3571–3586, Jun. 2021.

[18] J. P. Delmas, M. N. El Korso, H. Gazzah, and M. Castella, "CRB analysis of planar antenna arrays for optimizing near-field source localization," *Signal Process.*, vol. 127, pp. 117–134, 2016. [Online]. Available: https://www.sciencedirect.com/science/article/pii/S0165168416000815

[19] J.-P. Le Cadre, "Performance analysis of wavefront curvature methods for range estimation of a moving source," *IEEE Trans. Aerosp. Electron. Syst.*, vol. 31, no. 3, pp. 1082–1103, Jul. 1995.

[20] E. Grosicki, K. Abed-Meraim, and Y. Hua, "A weighted linear prediction method for near-field source localization," *IEEE Trans. Signal Process.*, vol. 53, no. 10, pp. 3651–3660, Oct. 2005.

[21] M. N. El Korso, A. Renaux, R. Boyer, and S. Marcos, "Deterministic performance bounds on the mean square error for near field source localization," *IEEE Trans. Signal Process.*, vol. 61, no. 4, pp. 871–877, Feb. 2013.

[22] S. Zhang, T. Jost, R. Pöhlmann, A. Dammann, D. Shutin, and P. A. Hoeher, "Spherical wave positioning based on curvature of arrival by an antenna array," *IEEE Wireless Commun. Lett.*, vol. 8, no. 2, pp. 504–507, Apr. 2019.

[23] X. Yin, S. Wang, N. Zhang, and B. Ai, "Scatterer localization using large-scale antenna arrays based on a spherical wave-front parametric model," *IEEE Trans. Wireless Commun.*, vol. 16, no. 10, pp. 6543–6556, Oct. 2017.
[24] A. Guerra, F. Guidi, D. Dardari, and P. M. Djuric, "Near-field tracking with large antenna arrays: Fundamental limits and practical algorithms," *IEEE Trans. Signal Process.*, vol. 69, pp. 5723–5738, 2021.
[25] S. J. Orfanidis, "Electromagnetic waves and antennas," 2008. [Online]. Available: http://www.ece.rutgers.edu/orfanidi/ewa/
[26] O. Tsilipakos et al., "Toward intelligent metasurfaces: The progress from globally tunable metasurfaces to software-defined metasurfaces with an embedded network of controllers," *Adv. Optimal Mater.*, vol. 8, 2020, Art. no. 2000783.
[27] W. C. Chew, *Waves and Fields in Inhomogenous Media*. Hoboken, NJ, USA: Wiley, 1995.
[28] A. S. Y. Poon, R. W. Brodersen, and D. N. C. Tse, "Degrees of freedom in multiple-antenna channels: A signal space approach," *IEEE Trans. Inf. Theory*, vol. 51, no. 2, pp. 523–536, Feb. 2005.
[29] M. A. Jensen and J. W. Wallace, "Capacity of the continuous-space electromagnetic channel," *IEEE Trans. Antennas Propag.*, vol. 56, no. 2, pp. 524–531, Feb. 2008.
[30] F. K. Gruber and E. A. Marengo, "New aspects of electromagnetic information theory for wireless and antenna systems," *IEEE Trans. Antennas Propag.*, vol. 56, no. 11, pp. 3470–3484, Nov. 2008.
[31] S. M. Kay, *Fundamentals of Statistical Signal Processing: Estimation Theory*. Englewood Cliff, NJ, USA: Prentice Hall, 1993.
[32] K. Witrisal et al., "High-accuracy localization for assisted living: 5G systems will turn multipath channels from foe to friend," *IEEE Signal Process. Mag.*, vol. 33, no. 2, pp. 59–70, Mar. 2016.
[33] H. White, "Maximum likelihood estimation of misspecified models," *Econometrica: J. Econometric Soc.*, vol. 50, pp. 1–25, 1982.
[34] C. D. Richmond and L. L. Horowitz, "Parameter bounds on estimation accuracy under model misspecification," *IEEE Trans. Signal Process.*, vol. 63, no. 9, pp. 2263–2278, May 2015.
[35] S. Fortunati, F. Gini, M. S. Greco, and C. D. Richmond, "Performance bounds for parameter estimation under misspecified models: Fundamental findings and applications," *IEEE Signal Process. Mag.*, vol. 34, no. 6, pp. 142–157, Nov. 2017.

Antonio A. D'Amico received the Dr. Ing. degree in electronic engineering and the Ph.D. degree from the University of Pisa, Pisa, Italy, in 1992 and 1997, respectively. He is currently an Associate Professor with the Department of Information Engineering, University of Pisa. His research interests include digital communication theory, with emphasis on synchronization algorithms, channel estimation, and detection techniques.

Andrea de Jesus Torres (Member, IEEE) received the M.Sc. degree in telecommunications engineering in 2019 from the University of Pisa, Pisa, Italy, where he is currently working toward the Ph.D. degree with the Department of Information Engineering, University of Pisa. He is defending his thesis in March 2023. His research interests include communication theory, wireless communications, and electromagnetic theory, with main emphasis on reconfigurable intelligent surfaces, and holographic MIMO.

Luca Sanguinetti (Senior Member, IEEE) received the Laurea Telecommunications Engineer degree (*cum laude*) and the Ph.D. degree in information engineering from the University of Pisa, Pisa, Italy, in 2002 and 2005, respectively. In 2004, he was a Visiting Ph.D. Student with the German Aerospace Center (DLR), Oberpfaffenhofen, Germany. During June 2007 – June 2008, he was a Postdoctoral Associate with the Department Electrical Engineering, Princeton, NJ, USA. From July 2013 to October 2017, he was with Large Systems and Networks Group (LANEAS), CentraleSupélec, France. He is currently an Associate Professor with the Dipartimento di Ingegneria dell'Informazione of the University of Pisa. He has coauthored the textbooks *Massive MIMO Networks: Spectral, Energy, and Hardware Efficiency* (2017) and *Foundations on User-centric Cell-free Massive MIMO* (2020). He was an Associate Editor for the IEEE TRANSACTIONS ON WIRELESS COMMUNICATIONS and IEEE SIGNAL PROCESSING LETTERS, and the Lead Guest Editor of the IEEE JOURNAL ON SELECTED AREAS OF COMMUNICATIONS Special Issue on Game Theory for Networks and as an Associate Editor for the IEEE JOURNAL ON SELECTED AREAS OF COMMUNICATIONS (series on Green Communications and Networking). He is currently an Associate Editor for the IEEE TRANSACTIONS ON COMMUNICATIONS and is a Member of the Executive Editorial Committee of IEEE TRANSACTIONS ON WIRELESS COMMUNICATIONS. His expertise and general interests include communications and signal processing. He was the recipient of the *2018 and 2022 Marconi Prize Paper Awards in Wireless Communications* and coauthored a paper that received the Young Best Paper Award from the ComSoc/VTS Italy Section. He was the corecipient of Two Best Conference Paper Awards: *IEEE WCNC 2013* and *IEEE WCNC 2014*. He was also the recipient of the FP7 Marie Curie IEF 2013 Dense deployments for green cellular networks.

Moe Z. Win (Fellow, IEEE) is currently a Professor with the Massachusetts Institute of Technology (MIT), Cambridge, MA, USA, and the Founding Director of the Wireless Information and Network Sciences Laboratory. Prior to joining MIT, he was with AT&T Research Laboratories and with NASA Jet Propulsion Laboratory. His research interests include fundamental theories, algorithm design, and network experimentation for a broad range of real-world problems. His current research interests include ultra-wideband systems, network localization and navigation, network interference exploitation, and quantum information science. He was the IEEE Communications Society as an elected Member-at-Large on the Board of Governors, as the elected Chair of the Radio Communications Committee, and an IEEE Distinguished Lecturer. Over the last two decades, he held various editorial positions for IEEE journals and organized numerous international conferences. He was on the SIAM Diversity Advisory Committee. He is an elected Fellow of the AAAS, the EURASIP, and IET. He was honored with two IEEE Technical Field Awards: the IEEE Kiyo Tomiyasu Award in 2011 and the IEEE Eric E. Sumner Award in 2006, jointly with R. A. Scholtz. His publications, coauthored with students and colleagues, have received several awards. Other recognitions include the MIT Everett Moore Baker Award in 2022, the IEEE Vehicular Technology Society James Evans Avant Garde Award in 2022, the IEEE Communications Society Edwin H. Armstrong Achievement Award in 2016, the Cristoforo Colombo International Prize for Communications in 2013, the Copernicus Fellowship in 2011, and the *Laurea Honoris Causa* in 2008 from the Università degli Studi di Ferrara, and the U.S. Presidential Early Career Award for Scientists and Engineers in 2004. He is an ISI Highly Cited Researcher.

Open Access provided by 'Università di Pisa' within the CRUI CARE Agreement.